8-2024

Local Charge Distortion due to Cr in Ni-based Concentrated Alloys

Jacob Fischer
Clemson University, jwfisch@clemson.edu

8-2024

Local Charge Distortion due to Cr in Ni-based Concentrated Alloys

Jacob Fischer
Clemson University, jwfisch@clemson.edu

LOCAL CHARGE DISTORTION DUE TO Cr IN Ni-BASED CONCENTRATED ALLOYS

A Thesis
Presented to
the Graduate School of
Clemson University

In Partial Fulfillment
of the Requirements for the Degree
Masters of Science
Materials Science and Engineering

---

by
Jacob Fischer
August 2024

Accepted by:
Dr. Dilpuneet Aidhy, Committee Chair
Dr. Enrique Martinez-Saez
Dr. Garrett Pataky

ABSTRACT

Due to the presence of multiple elements consisting of a range of atomic radii, local lattice distortion (LLD) is commonly observed in concentrated (and high entropy) alloys. However, since these elements also have diverse electronegativities, recent works show that atoms can have a range of atomic charges. In this work, using density functional theory (DFT), we investigate electronic charge distribution in face centered cubic (FCC) Ni-based alloys and find significant charge-density distortion in HEAs. Specifically, Cr atoms have large charge density distortion that results in a wide range of bond lengths, atomic charges, and electronic density of states in Cr-containing alloys. The charge distortion impacts the stacking fault energies (SFEs) as a wide range of SFEs are observed in Cr-containing alloys (e.g., NiCr, NiFeCr and NiCoCr), which are otherwise narrow and converged in non-Cr containing alloys such as NiFe, NiCo and NiFeCo. These observations provide insights into the role of local charge distortion towards local lattice distortion in HEAs and illustrate the effect of charge distortion on the mechanical properties of the alloys.

DEDICATION

Dedicated to my family who have always been there to encourage me throughout my academic career. You have constantly supported and inspired me to do my best. I am truly thankful to have such a wonderful family and I love you always.

ACKNOWLEDGMENTS

First I would like to thank my advisor, Dr. Dilpuneet S. Aidhy, for his support, patience, and encouragement throughout my studies. I am grateful to him for pushing me to develop a more well-rounded and professional approach to research.

I would like to thank my committee members Dr. Enrique Martinez-Saez and Dr. Garrett Pataky for agreeing to be on my committee and meeting with me to discuss my research.

I would like to thank the National Science Foundation for their support during my research project.

I would also like to thank the Department of Materials Science and Engineering at Clemson University for their continous support throughout my undergraduate and graduate career.

TABLE OF CONTENTS

Page

Table of Contents (Continued) Page

LIST OF TABLES

LIST OF FIGURES

List of Figures (Continued)

Figure Page

List of Figures (Continued)

Figure Page

List of Figures (Continued)

Figure Page

CHAPTER ONE: INTRODUCTION

1.1 Background

Traditionally, alloys consist of one primary base element and smaller concentrations of other alloying elements to improve material performance [1]. This method, while effective, is hindered by its limited compositional space and leaves little to no knowledge about alloys containing three or more main components [6]. The expectation was that multicomponent alloys would form intermetallic compounds with complex microstructures, resulting in brittleness, processing difficulties, and challenges in characterization analysis [7]. However, in the early 21st century it was discovered that single-solid solution phases could be obtained from structures with multiple principal elements at near-equimolar ratios [7,8]. This new strategy for designing alloys shifted the focus toward more chemically complex materials that exhibit unique properties [9].

Originally, these new alloys were called “high entropy alloys” (HEAs) due to their high configurational entropy from randomly mixing multiple elements in high concentrations [1]. This configurational entropy can be expressed as:

$$\Delta S_{conf} = RlnN \quad (1)$$

where R is the gas constant (8.31 J/K mol), and N is the total number of different elements [10]. As shown in Figure 1, the configurational entropy of mixing of an alloy is equivalent to an ideal gas and this value will be maximized in an equiatomic composition [1].

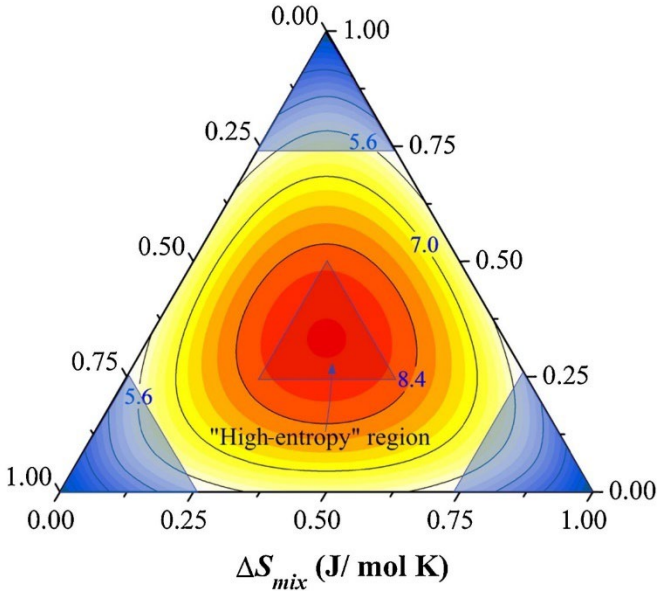

Figure 1. Contour plot of the ΔS_{mix} for a ternary alloy system. The blue corners represent the design space of conventional alloys while the red-center indicates the "high-entropy region." [1]

HEAs are also defined by four core effects based on their kinetics, thermodynamics, and atomic structure which influence the development of the microstructure. One such effect is the high entropy effect which states that the high configurational entropy of HEAs reduces the Gibbs free energy of the single solid phase solution, making it more stable compared to intermetallic phases [2]. However, recent studies have shown that a large number of multiphase alloys (containing intermetallic compounds and metallic glasses) were created using the methodology proposed in Eqn. 1 [9]. Upon further investigation by other research groups, it was determined that the configurational entropy mixing is not the sole contributor responsible for the unique material properties and atomic structure of these alloys [1]. The continuous examination of just one of these core effects

demonstrates that these exceptional alloys have their own unique mechanisms that drive their own design. Since the initial proposal of the four core effects by Yeh et al. [7], numerous studies have continuously analyzed and refined these concepts. This ongoing research includes providing evidence that supports, challenges, or builds upon the high entropy effect, sluggish diffusion effect, severe lattice distortion, and cocktail effect [11]. For the scope of this work, we will focus on the severe lattice distortion core effect caused by the chemical complexity of HEAs.

1.2 Local Lattice Distortion

The chemical randomness in HEAs, characterized by the random distribution of elements on the crystal lattice, leads to a wide variety of distinct nearest-neighbor (NN) environments. Additionally, the disparity among the atomic radii of the elements leads to the displacement of atoms from their ideal lattice sites creating bond length variations. The NN environment and atomic radii collectively lead to a distorted lattice, as shown in Figure 2. This phenomenon is known as local lattice distortion (LLD), which has been observed both experimentally and computationally [12–14]. These localized distortions interact elastically with dislocations moving through the lattice, resulting in solid solution strengthening [2,15]. Mo et al. [16] observed that increasing the Hf content in a $NbMoTaWHf_x$ alloy leads to a simultaneous increase in both compressive strength and failure strain up to $Hf_{0.92.}$ The study by Mo et al. [16] also highlights that this same concentration of Hf exhibited one of the highest mean absolute atomic

displacements (MAAD), which is another common way to measure LLD. A similar study by Liu et al. [17] demonstrated increasing the LLD resulted in a monotonic increase in both yield strength and microhardness. Notably, NiCoMnCr and NiCoCr exhibited particularly high yield strengths.

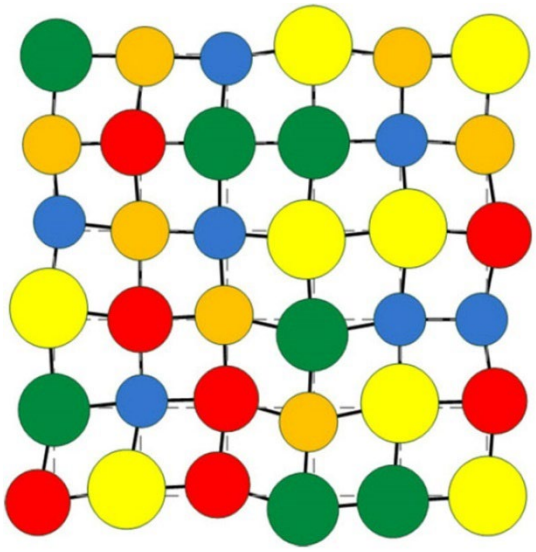

Figure 2. Local lattice distortion in HEAs. [2]

In fact, several studies have suggested that the severity of the LLD present in HEA alloys significantly contribute to its unique properties [3,18–20]. One way to quantify the atomic distortion is to use a statistical mechanics method known as mean-square atomic displacement (MSAD) which measures how far an atom deviates from its initial position. Okamoto et al. [3] calculated MSAD the elements encompassing the CrMnFeCoNi HEA (Cantor alloy) structure using DFT. Their results found that Cr and Mn exhibit the largest MSAD in the quaternary and quinary alloys as illustrated in Figure 3. These results agree with those found by Oh et al. [21] where Cr and Mn demonstrate the largest fluctuations in local bond

distortion consistently in theoretical and experimental data. It was reasoned that the large atomic size mismatch of the alloy components is the main contributor to

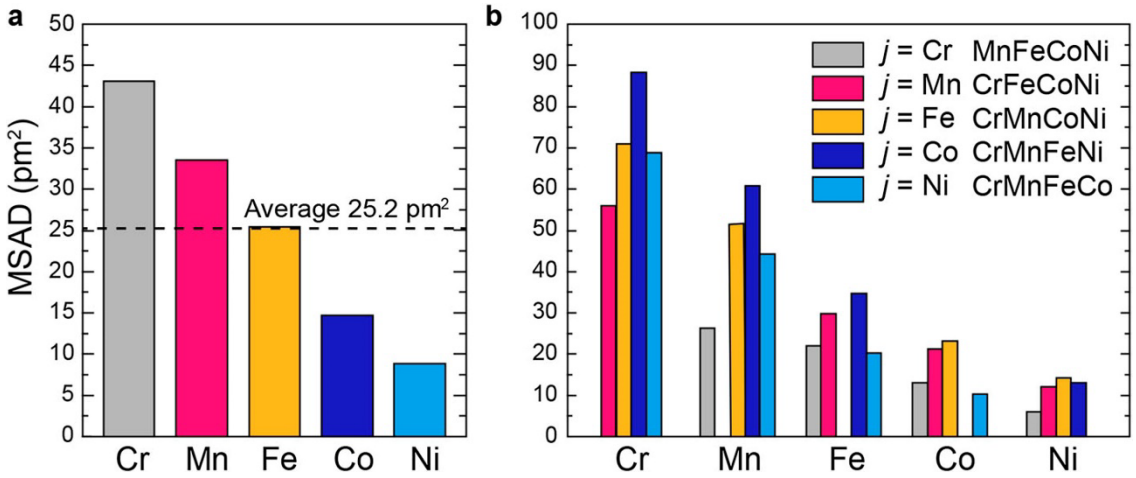

Figure 3. MSAD of each of the constituent elements. (a) Quinary CrMnFeCoNi HEA, and (b) five different quaternary equiatomic alloys derived by first-principles total-energy calculations for SQSs with the 5×5×4 and 4×4×4 FCC supercells, respectively. [3]

the severe lattice distortion observed in these alloys. However, studies have shown that the atomic size mismatch is not enough to accurately predict the LLD, and other factors need to be considered [4,19,22].

Recent DFT calculations have further revealed that due to the range of electronegativities of various alloying elements, different atoms of a given element experience different amounts of charge transfers that cause variations in their atomic radii [23]. The DFT calculations also suggest that the atomic displacement is closely linked to the charge transfer. For example, it has been shown that the elements that gain electrons have smaller atomic displacements and vice versa [24]. Thus, there is an emerging understanding that the atomic radius and charge transfer collectively lead to LLD**.** Tong et al. [19] demonstrate the effect of charge

transfer and how it alters the atomic radius of the constituent elements. This reduces the atomic size mismatch and stabilizes the energetically unfavorable severe LLD. A similar study by Oh et al. [4] made a direct relation between the charge transfer and the atomic displacement of an individual atom. As shown in Figure 4, elements with positive Bader charges have large atomic displacements whereas elements with negative Bader charges exhibit small atomic displacements.

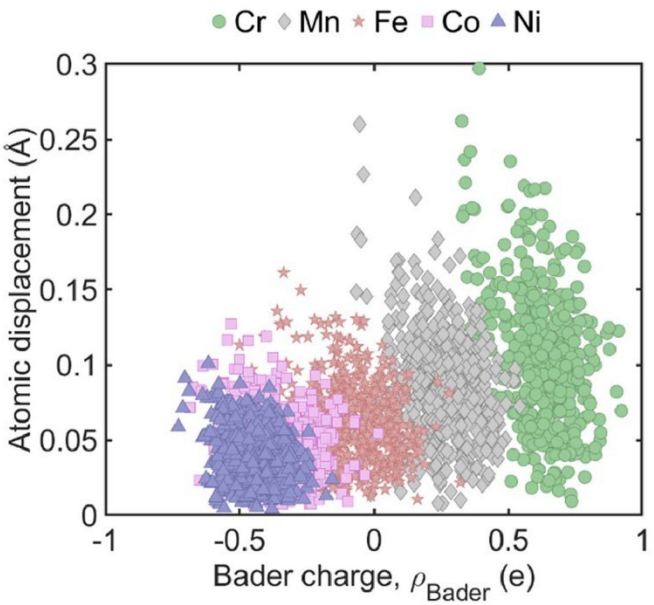

Figure 4. Atomic displacement versus Bader charge (positive: losing electrons) relation. [4]

1.3 Stacking Fault Energy

Recent studies have demonstrated that certain FCC HEAs, like NiCoCr, have a strong preference for the hexagonal-close-pack (HCP) structure at lower temperatures suggesting that the creation of stacking faults is energetically

favorable [25–28]. Stacking faults are generated when perfect dislocations dissociate into partial dislocations to reduce the elastic strain energy corresponding to Frank's Rule [29]. These defects disrupt the regular stacking sequence of atomic planes within the crystal lattice. Two main types of stacking fault exist: intrinsic and extrinsic. Intrinsic stacking faults disrupt the atomic arrangement by removing one atomic layer, creating a single break in the stacking sequence [29]. In contrast, extrinsic stacking faults introduce an extra layer, causing two disruptions in the sequence [29].

The introduction of a stacking fault results in a higher energy state compared to the perfect crystal. This energy difference per unit area is known as the stacking fault energy (SFE). Additionally, SFE measures the energy cost for shearing one atomic plane with respect to another, directly linking it to how a material deforms. Understanding SFE becomes crucial in HEAs, as the interplay between alloying elements and SFE significantly influences the competing deformation mechanisms. Low SFE is known to promote the formation of deformation twins leading to materials that exhibit excellent mechanical properties. For instance, Liu et al. [30] reported that among the alloys they studied, NiCoCr had the lowest SFE and exhibited the best combination of strength and ductility at room temperature. Due to the random presence of multiple elements, a range of defect energies are observed in each HEA due to lack of chemical symmetry in contrast to a rather unique (or narrow) value in a pure or dilute alloy. This significant difference can be attributed to several factors, including the complex interplay of

atomic sizes and electronic interactions within HEAs. The distribution of charge density, which we will discuss further in the next section, plays a crucial role in large SFE variations observed in various HEAs including NiCoCr.

1.4 Charge Transfer

Although charge transfer is normally quantified as a scalar value (e.g., via Bader segmentation in DFT), the spatial distribution of the electronic charge, especially its asymmetric distribution, emerges as an important parameter in the chemically random environments. This asymmetric distribution leads to localized distortions in the charge density, a phenomenon we refer to as local charge distortion (LCD). The charge distortion has been used to explain many properties including SFEs in alloys [31]. Zhao et al. [31] investigated the relationship between the local atomic arrangement and the SFE of concentrated solid-solution alloys by characterizing the charge density redistribution at bond critical points [31]. These bond critical points represent regions of high electron density between bonded atoms and are shown to influence the local variation in SFE. It has been postulated that large variations in SFEs can be attributed to the asymmetric charge distribution that could impose resistance to planar shearing in specific crystallographic directions [32–36]. Generally, denser charge density is associated with stronger bonding and a non-spherical distribution will hinder the shear deformation causing larger SFE [32]. Shang et al. [32] observe this in Ni-based super alloys where structures that exhibited an asymmetrical distribution of charge density after undergoing shear deformation had higher SFEs. Charge distortion

has also been used to explain unintuitive vacancy diffusion in metals [37] where, unintuitively, larger atoms have lower migration barriers due to easier charge reorientation at the saddle point. In addition, charge distribution is often used as a descriptor to probe surface/catalytic properties [38–40]. Previous work by Arora et al. [41,42] indicates an enhanced asymmetric charge distribution around Cr atoms in binary and ternary Ni-based model alloys compared to other elements. The underlying reason is likely the partially filled *d*-shell electron of Cr granting greater electronic deformation flexibility [43]. Zhao et al. [43] demonstrates that this enhanced flexibility induces larger variations of Cr point-defect energies compared to Ni and Co.

1.5 Motivation

Motivated by these observations, in this work, we examine LCD in Ni-based binary and ternary alloys in Ni-Fe-Co-Cr compositional space using DFT calculations. This thesis examines the relationship between electronic distortion and variations in SFE in both dilute and concentrated metallic alloys. Specifically, we show that (1) LLD and charge distortion are correlated, (2) there is much higher LCD around Cr atoms compared to other elements, (3) the presence of Cr causes much larger LLD, and (4) the larger LCD and LLD result in larger variations of SFEs. Based on these results, we propose that the amount of charge distortion is an important factor that affects the LLD and hence SFE. The alloys with symmetric charge distribution exhibit a narrow range of SFE in contrast to a larger variation in Cr-containing alloys.

CHAPTER TWO

CHAPTER TWO: METHODOLOGY

2.1 DFT Calculations

Density functional theory (DFT) is used to calculate both the charge density distribution and the SFE values for dilute and concentrated Ni-based alloys. The DFT calculations are performed using Vienna ab initio simulation package (VASP) code [44–46]. The full potential frozen-core project-augmented wave (PAW) is used to describe the electron-ion interactions along with the generalized gradient approximation (GGA) with Perdew-Burke-Ernzerhof (PBE) exchange correlation functional [47]. Figure 5a, 5b, and 5c displays the FCC supercells with a total of 108 atoms distributed on nine atomic layers. Figure 5a shows the 'dilute' structure containing only six alloying elements added only on the 5th layer. Figure 5b shows another dilute structure containing two different alloying elements, three atoms of each element in the 5th layer. Finally, Figure 5c is a concentrated special quasirandom structure (SQS) containing equiatomic ternary composition with alloying elements in all nine layers. The nine layers are parallel to the (111) plane and a 6 Å vacuum is applied to prevent the interaction between the top and bottom layers. The SQS structures are generated using the Alloy Theoretic Automated Toolkit (ATAT) software [48]. The Brillouin zone sampling is employed by the Monkhorst-Pack method with a $6 \times 6 \times 1$ k-point mesh. A plane wave energy cutoff of 350 eV is set, with total energy convergence within 1×10^{-4} eV and internal atomic position forces relaxed to less than 1×10^{-2} eV. The Methfessel-Paxton

method is implemented using a smearing width of 0.1 eV. Collinear spin-polarized calculations are performed with a ferromagnetic (FM) configuration. All atoms are initialized with a magnetic moment of LL. Both the dilute and SQS structures share this initial setup, but the magnetic moment of Cr exhibits a contrasting behavior once the final magnetic order has been determined. Upon relaxation, in dilute alloys, Cr adopts a FM alignment, deviating from its characteristic antiferromagnetic (AFM) behavior observed in the SQS structures. This shift in magnetic order is likely driven by the strong influence of the surrounding FM Ni atoms, which have high concentration compared to the Cr atoms that are sparsely distributed on the 5th layer of the dilute structure. Our findings agree with the observations of Niu et al. [25], who noted a strong influence of neighboring elements on Cr magnetic moments within NiCoCr and NiCoFeMnCr structures. Additionally, the final magnetic moment distributions for the SQS structures are also in good agreement with those obtained using established DFT methods [25,49–52]. This agreement includes the expected positive moments for Ni, Co, and Fe, while Cr exhibits a distribution of both positive and negative moments.

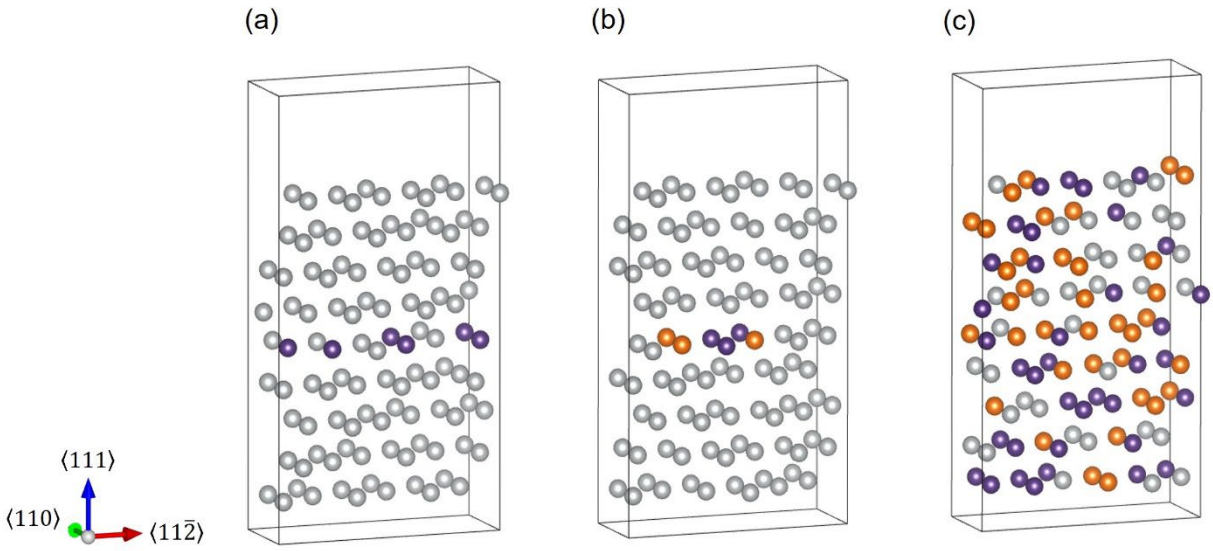

Figure 5. Supercells used for calculations of intrinsic SFEs in (a) dilute binaries (b) dilute ternaries, and (c) concentrated SQS ternary structures. Silver represents Ni host atoms while the orange and purple atoms are representative of the different alloying elements (Co, Fe, or Cr). In (a) and (b), alloying elements are added in the 5th layer only. See text for details.

2.2 Stacking fault energy

Goyal et al. [5] illustrate the two primary deformation mechanisms prevalent in FCC metals in Figure 6A and 6B. Figure 6A illustrates a simple slip deformation where layer A moves over to layer C along $\langle 110 \rangle$. In the case of Figure 6B, directly moving the atoms from layer A over to layer C has a high energy penalty. To overcome this steep energy barrier, the layer A atoms shift first to the positions within layer B, followed by a final shift to layer C. This creates a stacking fault region that is described by the Burgers vector equation:

$$\frac{1}{2}[\bar{1}10] = \frac{1}{6}[\bar{1}2\bar{1}] + \frac{1}{6}[\bar{2}11] \qquad (2)$$

where $\frac{1}{2}[\bar{1}10]$ is the Burgers vector for the full dislocation and $\frac{1}{6}[\bar{1}2\bar{1}]$ and $\frac{1}{6}[\bar{2}11]$ represent the Burgers vectors corresponding to the Shockley partial dislocations. A slab deformation approach is used to generate an intrinsic (ISF) along $\{111\}[11\bar{2}]$ for each supercell. The first four layers (from bottom to top) are fixed in their original position while the remaining layers are displaced in the $[11\bar{2}]$ direction creating an ISF along the 5th layer. Additionally, this leads to a change in the stacking sequence from *ABCABCABC* to *ABCACABCA*.

The initial bulk structure is first relaxed to fully optimize the atomic positions, cell shape, and cell volume of the supercell. Then, a vacuum is applied to both the perfect (non-sheared) and sheared structures for further relaxation, while constraining the cell shape volume. The SFE is then calculated using Eq. (2),

$$E_{SFE} = \frac{E_{sheared} - E_{perfect}}{A_{SF}} \quad (2)$$

where $E_{sheared}$ and $E_{perfect}$ are the energies for the perfect and sheared supercells, and A_{SF} is the cross-sectional area of the ISF. For the dilute structures, the host atoms on the 5th layer are substituted with various alloying atoms to calculate SFE using a standard method in literature [5,32,53,54]. In concentrated SQS structures, the SFE is calculated individually for each of the nine layers. Preliminary testing in pure Ni resulted in a calculated intrinsic SFE of 136.94 mJ/m^2, which is in good agreement with previous DFT results [32,55]. The calculated SFEs for concentrated ternary alloys in this study also fall within the range of values reported in prior literature [26,27].

The lengths of the lattice vectors **a**, **b**, and **c** of the orthorhombic cell are $a_0\sqrt{3/2}$, $a_0/\sqrt{2}$, and $a_0\sqrt{3}$ where a_0 is the lattice parameter of the FCC structure. The supercell is constructed with an initial lattice parameter of 3.52 Å, consistent with prior research [56,57]. Relaxation of the FCC unit cell converged to an average lattice constant of 3.514 Å, which falls within the range reported in previous studies [26,56–59]. Additionally, the converged average lattice constants for the NiFeCo, NiCoCr and NiFeCr concentrated alloys were found to be 3.547, 3.520, and 3.549 Å which are consistent with existing literature [26,60]. Multiple atomic configurations of both dilute structures (Figure 5a and 5b) are modeled to capture statistical variations. We recognize that the limited configurations do not encompass all possible configurations. However, they enable us to study the qualitative effect of Cr, which is the main goal of this work. We also acknowledge that magnetic fluctuations could possibly impact the observed SFE ranges, and our configurations may not capture a complete range of SFEs as this range can be very wide, observed in previous works [26,27,61].

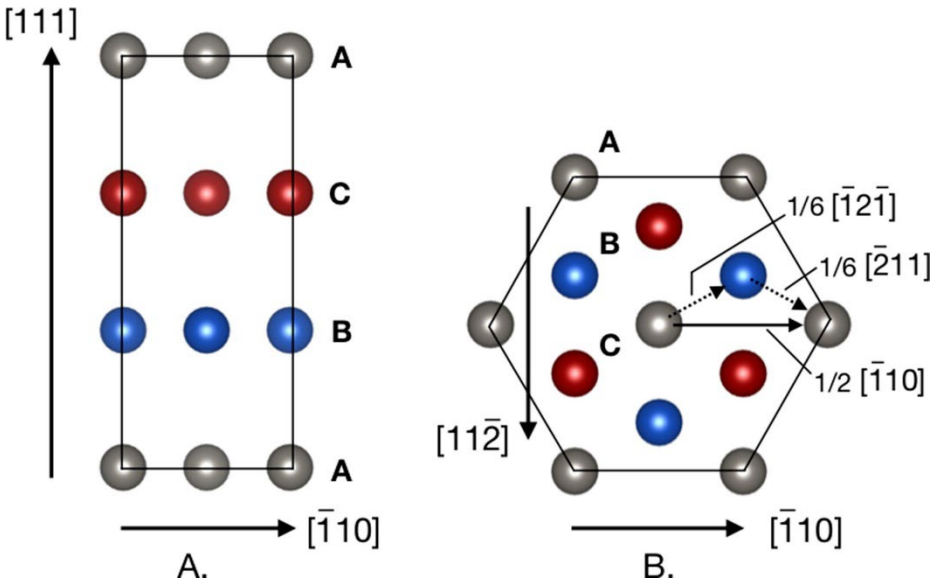

Figure 6. A. The geometry of the orthorhombic computational cell with three lattice vectors parallel to the $[11\bar{2}]$, $[\bar{1}10]$, and $[111]$ directions of the conventional FCC cubic unit cell. Atoms within this cell occupy the $\{111\}$ close packed planes with ABC stacking along $[111]$. B. Schematic showing atoms in the A layer sliding over the atoms in C layer along the perfect dislocation $\frac{1}{2}[\bar{1}10]$, which splits into two Shockley partial dislocations $\frac{1}{6}[\bar{2}11] + \frac{1}{6}[\bar{1}2\bar{1}]$. Atoms in the A, B and C layers are shown in grey, blue and red, respectively. [5]

2.3 Image processing of charge distortion

A key limitation identified by Arora et al. [42] is the qualitative nature of 2D contour plots used to visualize charge density distribution. This study utilizes image processing tools to quantify charge distortion, enabling a more objective and standardized comparison of data across different studies. The analysis of the charge distribution is performed by collecting charge density data from the CHGCAR file after full relaxation of the supercell. The data encompasses all layers normal to the $\langle 111 \rangle$ direction. For the dilute structures, we focus on the data from

the 5th layer to examine the charge distribution variations around the embedded alloying elements. In concentrated structures, all nine layers are analyzed. After data collection, contour plots are generated to visualize the charge density distribution within a chosen layer. Previous work in our group has used this technique to predict SFE using a convolutional neural network (CNN) model with charge density as a main descriptor [41,42]. In this work, we quantify the charge distortion via image processing.

The charge density images are prepared using a code from the sisl Python module [62]. The 800 x 500 pixel images display the distribution of charge at the center and surrounding an atom, as shown in Figure 7a and 7b. These images are processed using the open-source platform ImageJ/Fiji [63]. The software has been used to obtain quantitative data from images in other fields such as biology and medicine. For example, leveraging the functionality of ImageJ/Fiji, Pijuan et al. [64] assessed cell migration behavior to facilitate physiological and cellular characterization. It has also been utilized in materials science applications to analyze particles of varying sizes. For example, Boley et al. [65] use ImageJ to characterize the particle sizes of mechanically sintered Ga-In nanoparticles. In this study, we employ ImageJ/Fiji to quantify the charge distribution of the atoms to capture geometric changes that occur due to variations in LCD.

The images are first converted to an 8-bit grayscale with 256 levels of intensity. A threshold range is then set to separate the background area from the particle region. To capture the edges of the black region in Figure 7, the threshold

is manually set to exclude the red-yellow halo surrounding the completely visible atom in the middle of the image. Then, the ImageJ/Fiji's particle analysis package is used to compute the area of the concentrated charge that captures an accurate representation of the geometric variation occurring for each atom. The comparison of Figure 7a and 7b depicts the contrasting geometries that can occur in these alloys and highlights the extent of LCD. Figure 7c and 7d show an example of the processed image that is used to capture the area of the atoms. As shown later, a significant difference in the atomic area is observed for different elements, that is correlated to LLD.

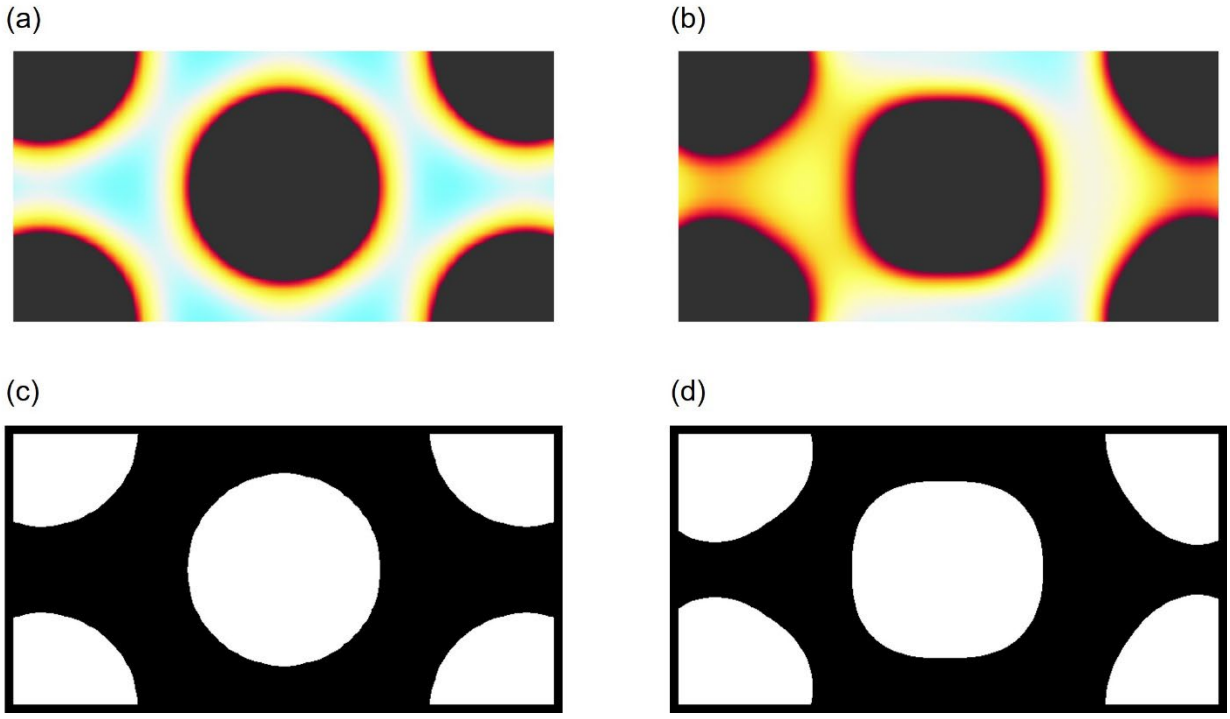

Figure 7. Preprocessed charge density images of (a) Ni and (b) Cr in a dilute NiCr alloy produced with sisl. (c) and (d) represent the converted grayscale images of Ni and Cr, respectively. These images are used to analyze the atomic charge and distortion, and to calculate the atomic area.

CHAPTER THREE: RESULTS

This study explores a variety of FCC crystal structures with different levels of chemical complexity. The dilute binary structures are used to confirm that significant LCD is specific to Cr-containing alloys. Additionally, in these binary dilute alloys, the arrangement of the non-Cr elements has no significant effect on the SFE variation. Dilute ternaries are employed to investigate the same concepts as the binary alloys. However, these ternaries introduce another alloying element to the structure to explore how even with additional chemical complexity, Cr-containing alloys exhibit the largest variations in bond length, Bader charge, and SFE. Finally, Concentrated alloys are analyzed to determine if the trends observed in dilute alloys persist. The expectation is that the Cr-containing alloys will exhibit the largest variations in LCD and SFE.

3.1 Charge density distortion in dilute binary alloys

The charge density distributions of the 5^{th} layer corresponding to Figure 5a in ten different supercells are shown in Figure 8. The corresponding SFEs calculated at the 5^{th} layer in all supercells are shown in Table 1. Note that each supercell consists of six atoms of an alloying element (i.e., either Co, Fe, or Cr) in the 5^{th} layer while the remaining atoms are all Ni. The only difference among the supercells is the arrangement of the alloying atoms during the initial setup to the DFT calculation. It is observed that all ten configurations in both NiCo and NiFe alloys display symmetrical charge distributions suggesting minimal LCD as shown in Figure 8a and 8b, respectively. In addition, there is an almost negligible

difference in the charge distribution between Ni and Co atoms, and there is subtle difference between Ni and Fe atoms. This uniform distribution sharply contrasts with NiCr alloys in Figure 8c, which display significant variations in charge density at three different levels: across ten configurations, between Ni and Cr atoms of a given configuration, and among Cr atoms of the same configuration. For example, the charge densities of configurations C2, C4, C6, C7, C8, C9 and C10 have larger variations whereas that in configurations C1, C3 and C5 show little to no variation. The configurations with high variation exhibit pronounced distortion around Cr atoms, indicative of larger LCD. In contrast, Ni atoms experience minimal distortion. While some Cr atoms appear circular (such as in C1 and C3), others exhibit an elliptical or even a quadrilateral geometry (such as in C6 and C9). Such wide variations and differences among the alloying elements are not observed in NiCo and NiFe. These results indicate that there is significant LCD around Cr atoms.

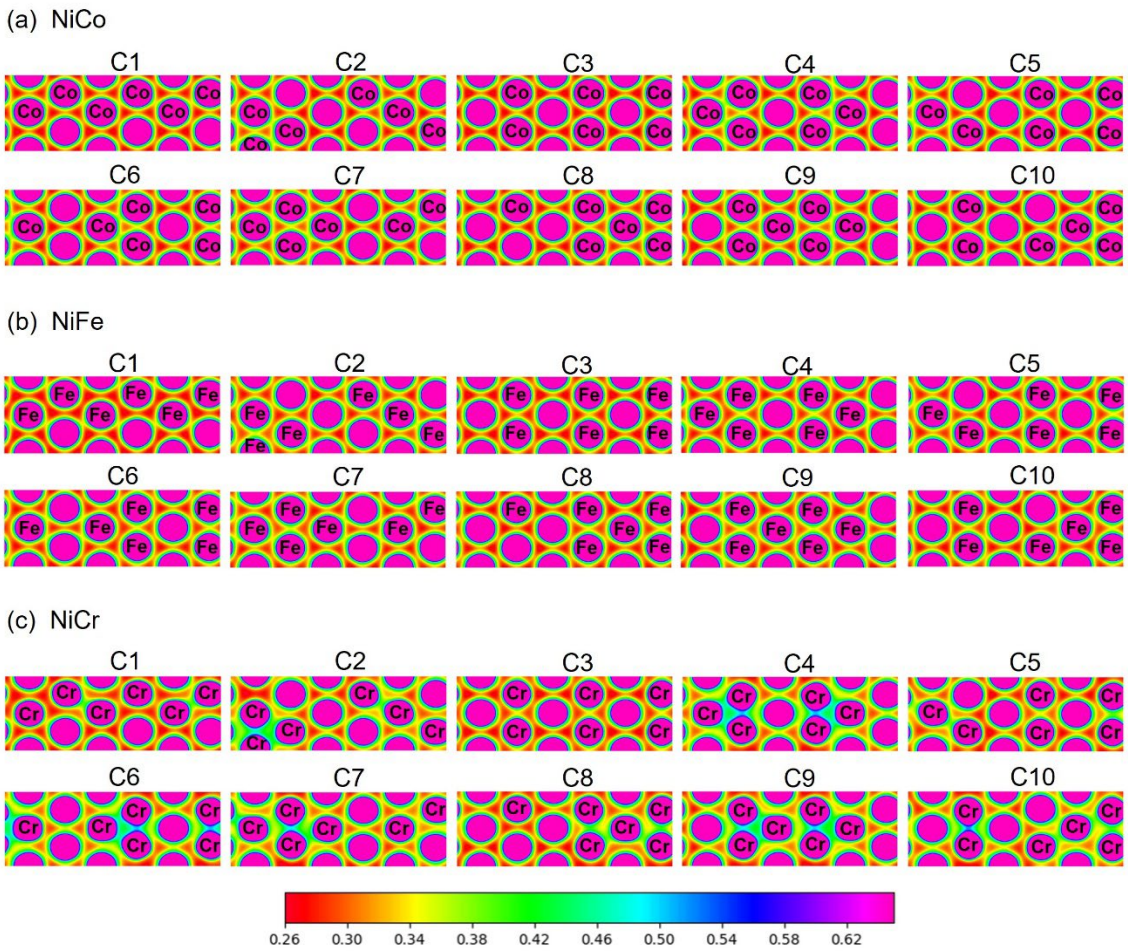

Figure 8. Charge density distribution in binary dilute alloys namely, (a) NiCo, (b) NiFe, and (c) NiCr. Each of the ten configurations have a total of six alloying atoms placed in the 5th layer. Unlabeled atoms are Ni. A higher charge distortion is observed in NiCr compared to NiFe and NiCo.

Table 1. SFE values for all ten configurations of NiCo, NiFe, and NiCr dilute binary alloys.

Configuration	NiCo (mJ/m^2)	NiFe (mJ/m^2)	NiCr (mJ/m^2)
C1	94.313	76.48	3.927
C2	96.625	73.657	56.003
C3	93.969	79.164	-16.859
C4	96.764	73.603	40.78
C5	95.981	75.556	62.243
C6	96.693	73.488	40.752
C7	94.756	72.357	26.717
C8	95.426	73.122	50.745
C9	96.64	70.678	51.763
C10	94.178	76.108	21.415

Interestingly, it is noted that there is a correlation between the LCD and SFE variation. While the SFE variation in NiCo and NiFe is small, i.e., with a standard deviation (σ) of ±1.1 mJ/m^2, NiCr exhibits a significantly larger spread with a σ of ±24 mJ/m^2 as shown in Table 1. The effect of LCD is further observed in the DOS of the alloying elements in each supercell, as shown in Figure 9. In NiCo, among all ten configurations, there is very little variation of the Co DOS at the Fermi level, as shown in Figure 9a, and there is minor variation among the Fe atoms, as shown in Figure 9b. Figure 9c, however, illustrates the diverse profiles of the Cr DOS in NiCr, reaffirming the larger charge density distortion. These results indicate that the configurational placement of alloying element is not the main cause of variations in the SFEs. Instead, the observed variations are attributed to the differences in charge density distribution.

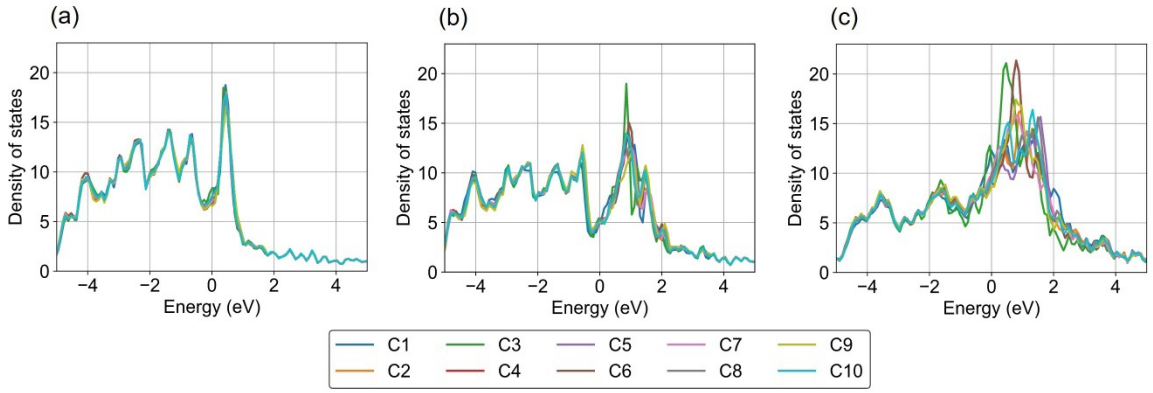

Figure 9. Projected DOS for (a) Fe and (b) Co atoms in NiFeCo, (c) Co and (d) Cr atoms in NiCoCr, and (e) Fe and (f) Cr atoms in NiFeCr in eight different configurations. The Fermi level is set to 0 eV for each alloy.

The LCD around Cr is also evidenced in the valence charge of the atoms quantified by Bader charge. Figure 10 shows the Bader charge distribution of all Co, Fe and Cr atoms among all ten configurations plotted against their respective SFEs. Due to the lowest electronegativity of Cr, it loses the largest amount of charge. The charge lost by Co and Fe atoms is relatively smaller, and because Co has higher electronegativity than Fe, they lose smaller charge than Fe atoms. In all alloys, the Ni atoms gain charge due to their highest electronegativity, as shown in Figure 10. The distribution of the Bader charges of the alloying elements illustrates charge distortion; while the Bader charges of Co and Fe atoms are similar and clustered, that of the Cr atoms is scattered, illustrating the variability of charge distribution around Cr atoms. The wider distribution of Ni Bader charges is only in NiCr structure and is due to the Bader charge distribution of the Cr atoms.

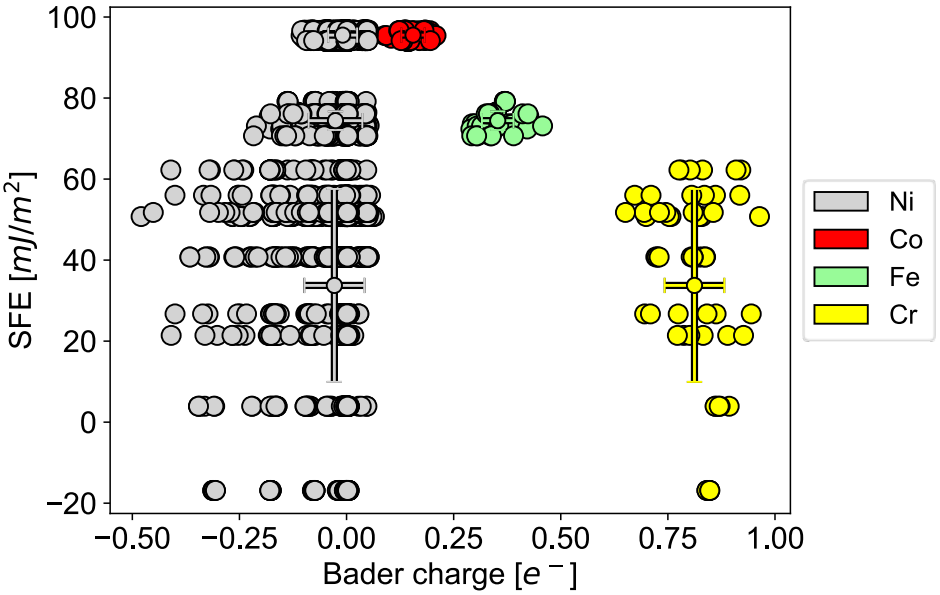

Figure 10. Bader charge of each atom in the ten supercells each of NiCo, NiFe and NiCr in Figure 1a. The corresponding SFEs of each supercell are also shown. Wide SFE and Bader charge variation in NiCr is observed compared to the NiFe and NiCo.

It is further observed that there is a correlation between LCD and LLD. Figure 11 shows the bond length distribution of all possible bonds in the three alloys. Figure 11a, 11b and 11c show Ni-Ni, Ni-X and X-X bond lengths in the three alloys, respectively, where X denotes Co, Fe or Cr. In NiCo and NiFe, a smaller variation among Ni-Ni bond lengths is observed; the σ of the variation is less than 0.007 Å, in Figure 11a. The σ is relatively higher in NiCr, i.e., 0.015 Å. In Figure 11b, the Ni-X bond length variation increases consistently in all three alloys compared to the corresponding Ni-Ni bonds. The variation is highest in Ni-Cr followed by Ni-Co and Ni-Fe. However, the X-X variation shows the most dramatic difference, as shown in Figure 11c. The Cr-Cr bonds have a very large variation (σ = 0.079 Å) compared to Co-Co and Fe-Fe bond lengths (σ = 0.014 Å and σ =

0.027 Å, respectively). These results reinforce the observation that Cr has much larger distortion in its NN environment compared to Co and Fe. In addition, collectively, Figure 9 and 10 indicate that LCD and LLD are likely corelated.

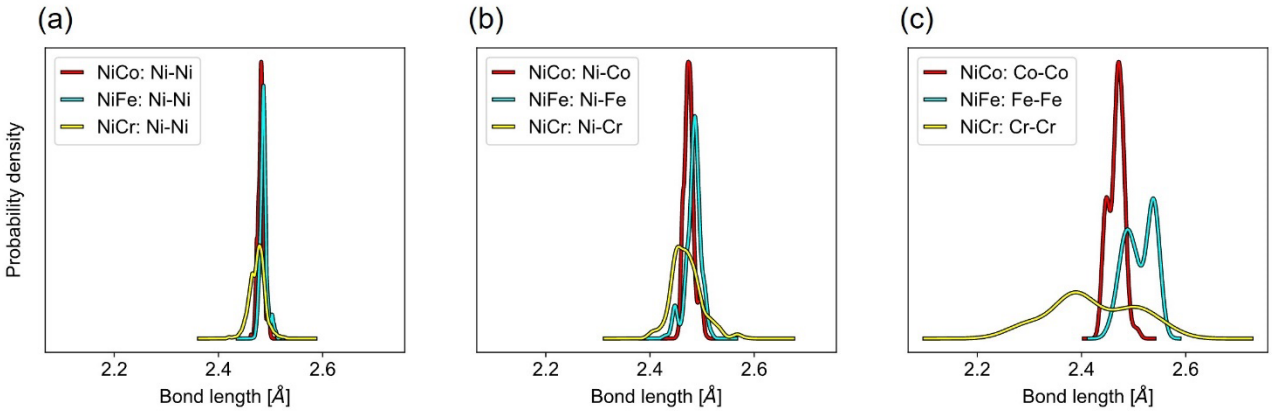

Figure 11. Bond length distributions in NiCo, NiFe, and NiCr dilute-binary structures. The bond lengths considered are the three 1NN bond types: (a) Ni-Ni, (b) Ni-X, (c) X-X, where X is the respective alloying element, Fe, Co or Cr in each alloy. Ni-Cr has a much larger bond length distribution, as observed in (c).

Even in very dilute structures, Cr has a profound effect on the charge-density distribution and SFEs. DFT calculations are performed in supercells containing only two alloying elements in the 5th layer. Two calculations for each alloying element are performed, distinguished by the placement of the atoms as the first nearest-neighbors (1NN) and third nearest-neighbors (3NN). The 3NN configuration is presumed to nullify (or reduce) the Cr-Cr interaction, within the constraints of the DFT supercell size. Among all three structures, the 3NN configuration has a lower total energy than 1NN which indicates that it is the preferred configuration. Minimal variation in both charge density and SFE is observed in Co and Fe structures in both 1NN or 3NN configurations as shown in Figure 12a and 12b, respectively. However, the structures containing Cr show a

significant difference in both local charge density and SFE. A higher charge density is observed between the two Cr atoms in the 1NN configuration as shown in Figure 12c. The DOS also reflects the trend observed for the atomic arrangements. Minimal variation is exhibited in the Co and Fe structures, while the Cr structures display larger difference. These results demonstrate that, even in the most dilute structures, the placement of Cr atoms can have a significant effect on its surrounding charge-density landscape.

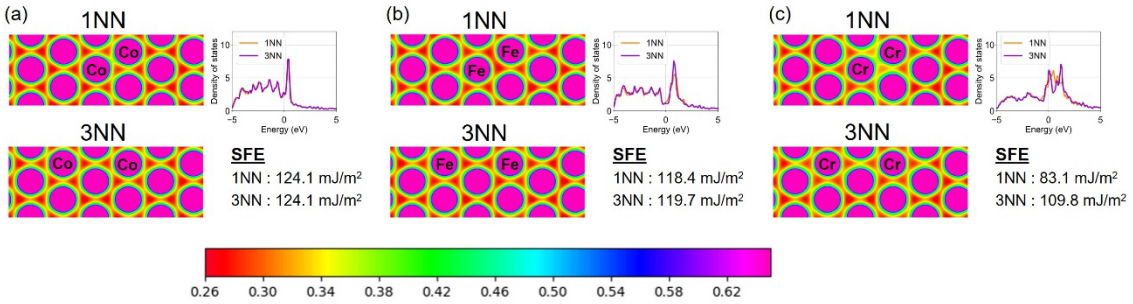

Figure 12. Comparison of charge density, DOS and SFE between 1NN and 3NN configurations in (a) NiCo, (b) NiFe, and (c) NiCr. Significantly higher variations for all three quantities are observed in NiCr.

3.2 Charge density distortion in dilute ternary alloys

To understand the effect of Cr in the presence of other alloying elements, three ternary alloys i.e., NiFeCo, NiCoCr, and NiFeCr are investigated. The supercells resemble binary structures, with alloying elements solely in the 5th layer. Three atoms of each alloying element are added, leading to a total of six alloying atoms. The charge density distributions of NiFeCo, NiCoCr, and NiFeCr are shown in Figure 13a, 13b and 13c, respectively. Consistent with previously discussed results, minor charge distortion is observed in NiFeCo in Figure 13a. Figure 13b

shows larger variations in the charge density distributions in NiCoCr with severe distortion around Cr-Cr bonds such as in configurations C1, C3 and C5. This charge distortion and Cr correlation becomes evident during comparison between NiFeCo and NiFeCr, as shown in Figure 13a and 13c, respectively. Although the Ni and Fe atoms have the same atomic placements in both structures, the charge density distributions are dissimilar. In NiFeCo, all eight configurations exhibit similar charge density distributions regardless of the arrangement of Fe and Co atoms. In contrast, the presence of Cr atoms in NiFeCr leads to larger LCD compared to NiFeCo. The configurations with more Cr-Cr bonds seem to coincide with larger LCD. This warrants further investigation pertaining to the influence of Cr-Cr bond interaction. Interestingly, the LCD is not confined to the immediate vicinity of Cr atoms indicating a more extensive spatial influence. The presence of Cr atoms disrupts the symmetrical charge density distribution, leading to more asymmetry around Ni and Fe atoms as well. The configurations C1, C3 and C5 display a particularly pronounced distortion. This increased distortion leads to a notable increase in LCD in Ni and other alloying elements, which becomes more evident in concentrated alloys presented later. Compared to non-Cr counterparts like NiFeCo, alloys containing Cr exhibit larger variations in SFE, as shown in Table 2.

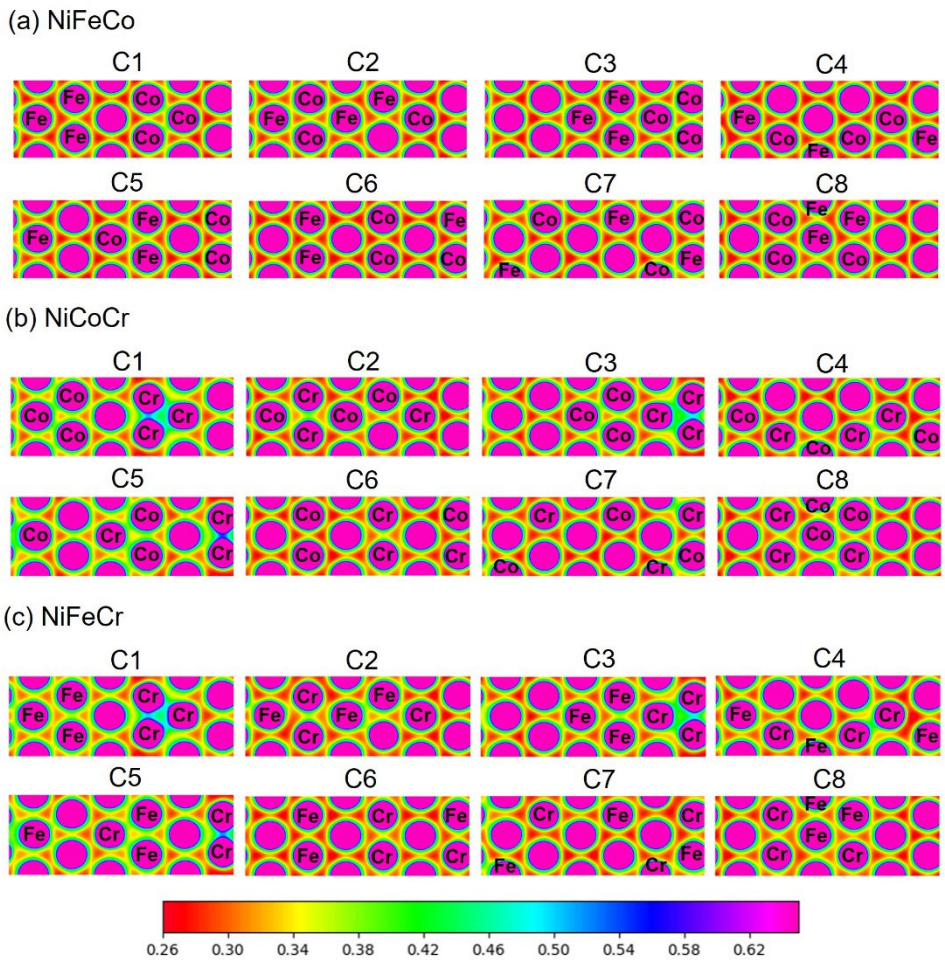

Figure 13. Charge density distributions in dilute ternary alloys: (a) NiFeCo, (b) NiCoCr, and (c) NiFeCr. Even with the addition of multiple alloying elements, alloys containing Cr display higher LCD. Areas in green and blue indicate areas of high charge density.

Table 2. SFE values for all eight configurations of NiFeCo, NiCoCr, and NiFeCr dilute ternary alloys.

Configuration	NiFeCo (mJ/m^2)	NiCoCr (mJ/m^2)	NiFeCr (mJ/m^2)
C1	85.992	77.023	68.118
C2	84.524	75.009	60.506
C3	81.922	62.505	52.527
C4	86.845	72.969	73.412
C5	85.155	72.803	-26.139
C6	87.664	41.417	-17.626
C7	84.595	71.828	48.171
C8	72.375	75.963	59.304

The DOS plots also show larger variation in Cr alloys, as shown in Figure 14. While little to moderate DOS variation occurs for Co and Fe atoms as observed in Figure 14a, 14b, 14c and 14e, a much larger variation is observed for Cr atoms, as shown in Figure 14d and 14f. This substantial DOS difference of Cr atoms indicates the presence of charge density distortion due to Cr even in multi-elemental alloys.

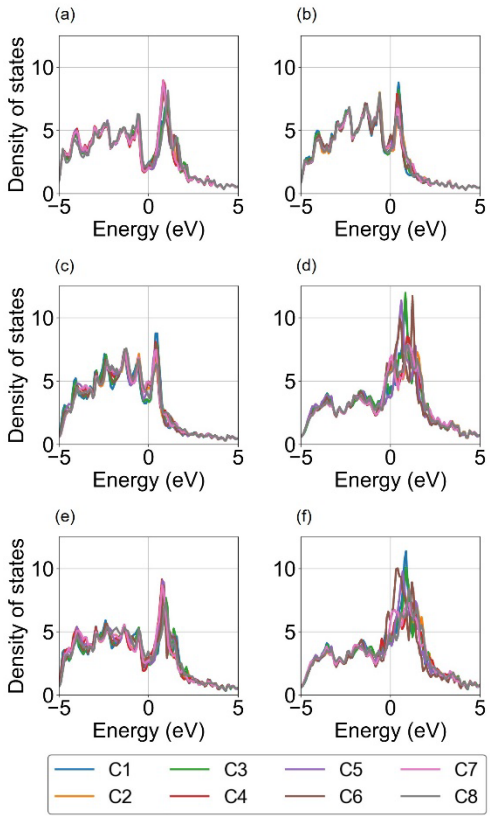

Figure 14. Projected DOS for (a) Fe and (b) Co atoms in NiFeCo, (c) Co and (d) Cr atoms in NiCoCr, and (e) Fe and (f) Cr atoms in NiFeCr in eight different configurations. The Fermi level is set to 0 eV for each alloy.

Figure 15 illustrates the Bader charge and SFE in the three structures. As demonstrated in binary compositions, the ternary compositions show larger Bader charge variation in Cr containing compositions NiFeCr and NiCoCr, whereas little variations are observed in NiFeCo. Similarly, there is greater SFE variation in the Cr-containing structures. The bond length variations, as illustrated in Figure 16, are likely a consequence of the observed charge distortions. For example, the Ni-Ni bonds in NiFeCo have a relatively narrower distribution (and higher peak) compared to the two Cr-containing compositions displayed in Figure 16a. Similarly,

the Ni-Fe bonds have wider variation in NiFeCr compared to NiFeCo, as shown in Figure 16b. Figure 16c shows that Ni-Cr bonds have larger distortion both in NiFeCr and NiCoCr compared to Ni-Co bonds in NiFeCo. The distribution of Co-Co and Fe-Fe bond lengths, shown in Figure 16d and 16e, exhibit smaller variation compared to Cr-Cr bonds. The Co-Cr and Fe-Cr bonds in Figure 16f demonstrate a larger distortion than Fe-Co bonds. These results are an initial indication that in multi-elemental alloys, Cr could demonstrate wider ranges across all bond types. We conclude that while the non-Cr compositions display moderate fluctuations due to LLD caused by atomic radii differences, the larger distortions observed in Cr-containing alloys are likely caused by the combined effect of LLD and LCD, and the latter has a significant contribution to the overall distortion.

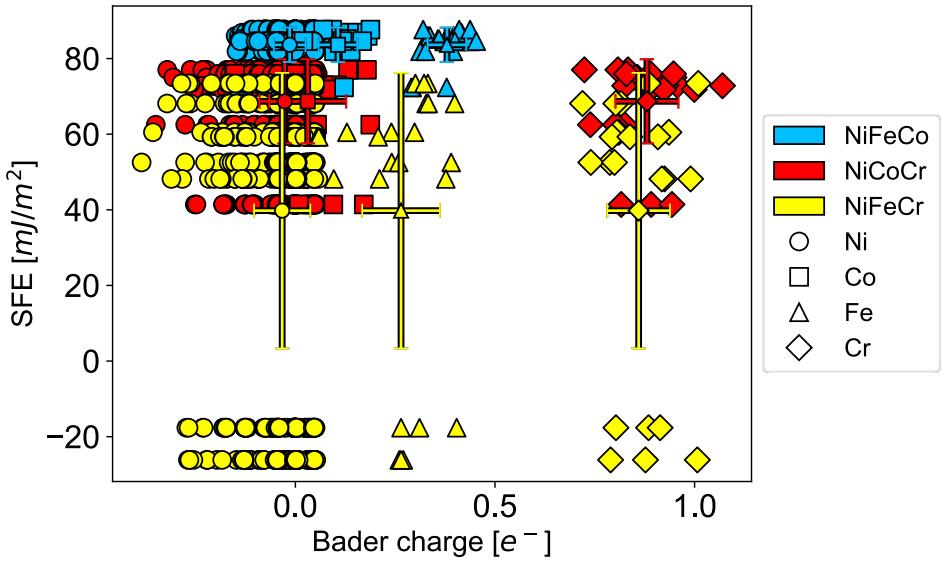

Figure 15. Bader charge of each atom in the eight configurations in NiFeCo, NiCoCr and NiFeCr with the corresponding supercell as shown in Figure 1b. The corresponding SFEs of each supercell are also shown. Wide SFE and Bader charge variation in NiFeCr and NiCoCr is observed compared NiFeCo.

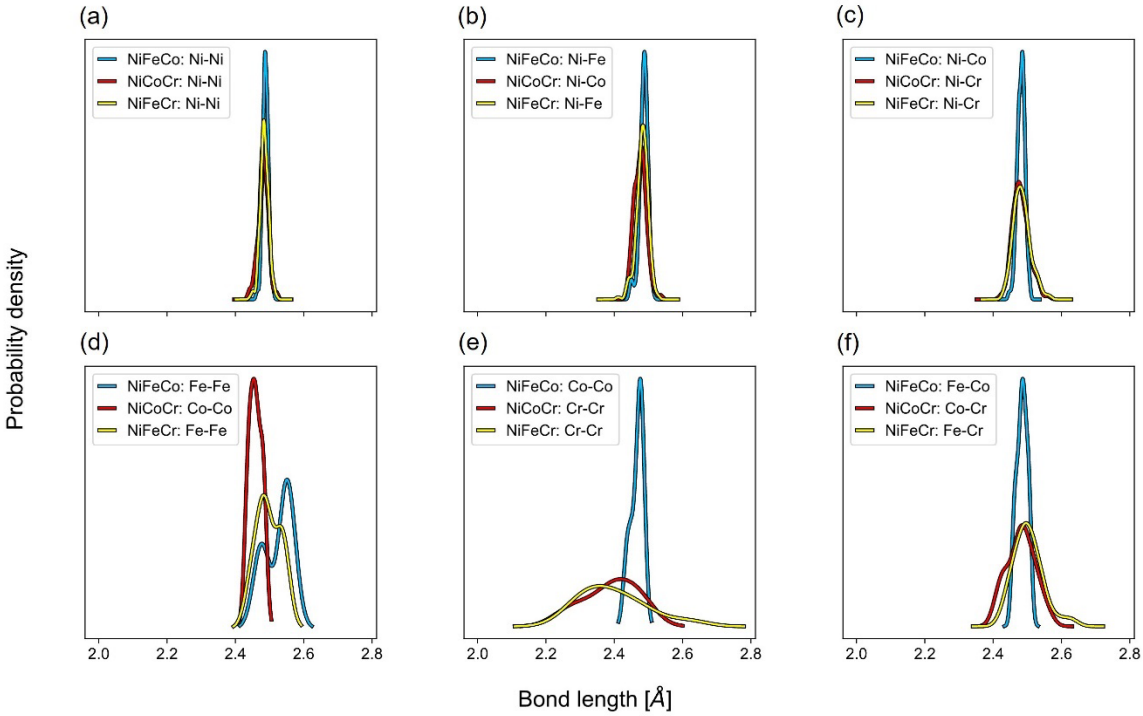

Figure 16. Bond length distribution for all dilute ternary alloys. Six 1NN bond types are considered for all structures: (a) Ni-Ni, (b) Ni-X_1, (c) Ni-X_2, (d) X_1-X_1, (e) X_2-X_2, (f) X_1-X_2 where X_1 and X_2 represent the distinct alloying elements for each structure.

3.3 Charge density distortion in concentrated ternary alloys

Finally, the charge density distortion is analyzed in concentrated equiatomic ternary alloys. The supercells consist of equal concentration of three elements in all nine layers constructed in SQS. The trends of lattice and charge distortions not only translate into SQS structures, i.e., the Cr containing alloys have larger bond length, Bader charge and SFE variations, but the variations are also more pronounced. The charge density distributions of all nine layers of each SQS structure of NiFeCo, NiCoCr, and NiFeCr are shown in Figure 17-19, and the corresponding SFEs are shown in Table 3. Smaller LCD is observed in Co and Fe

atoms, as shown in Figure 17. In contrast, the NiCoCr and NiFeCr structures demonstrate diverse charge distributions in each atomic layer and exhibit a wide range of SFEs that lie in both positive and negative range of values. Such variations in NiCoCr have been widely observed in previous DFT studies [26,27]. The LCD is more prevalent around Cr atoms and irregular shapes of Cr atoms are observed in Figure 18 and 19.

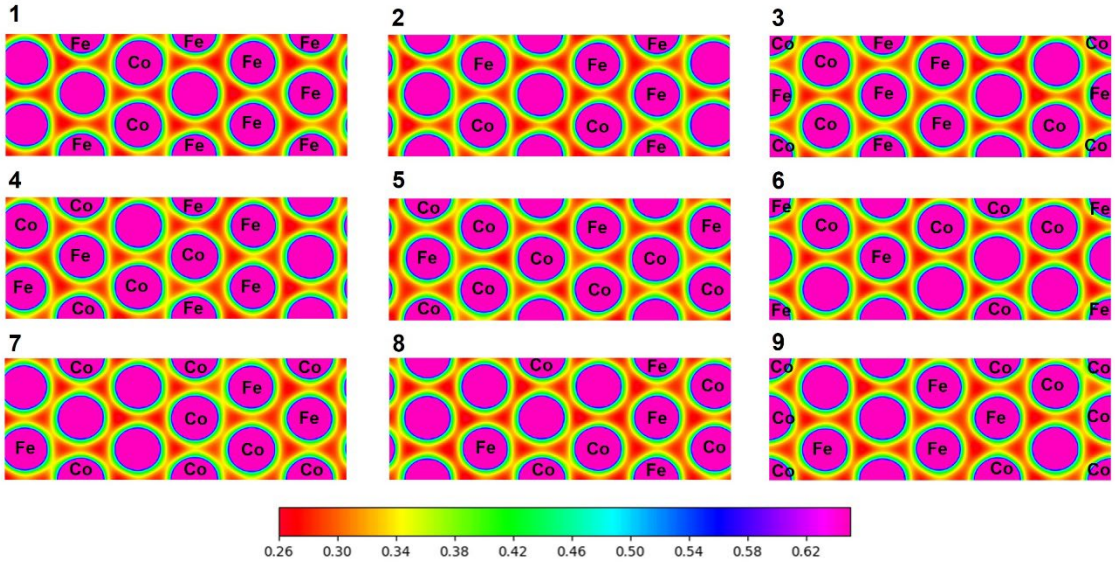

Figure 17. Charge density distributions of all nine layers in NiFeCo SQS ternary structure.

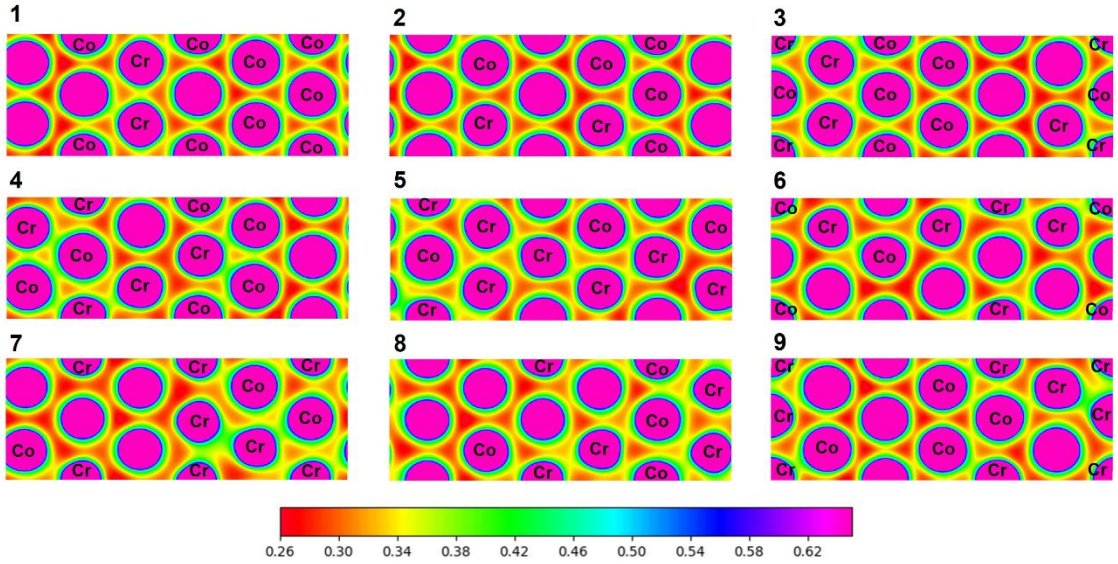

Figure 18. Charge density distributions of all nine layers in NiCoCr SQS ternary structure.

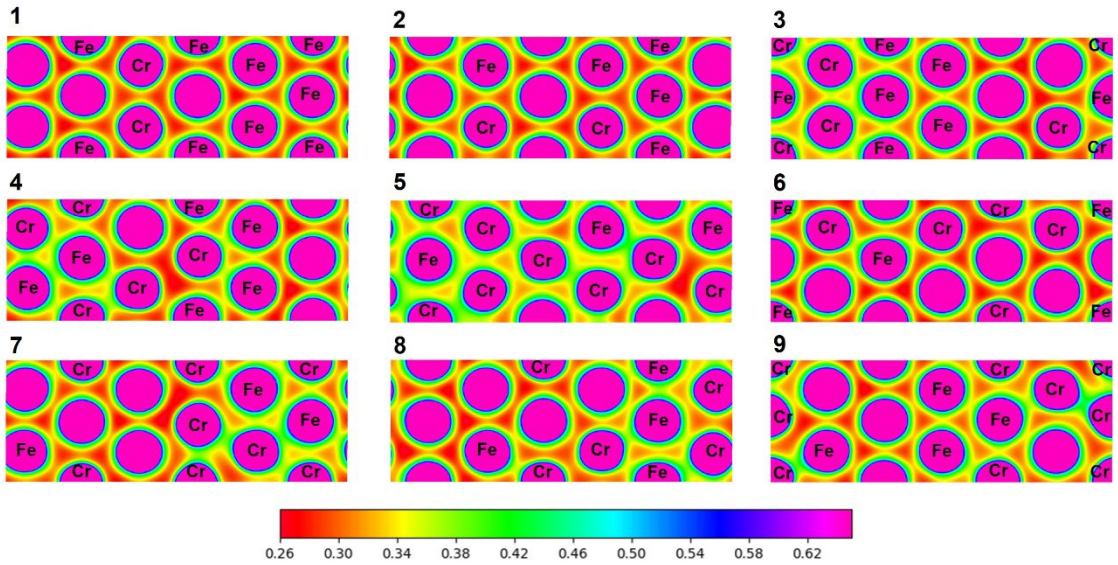

Figure 19. Charge density distributions of all nine layers in NiFeCr SQS ternary structure.

Table 3. SFE values for all nine layers of NiFeCo, NiCoCr, and NiFeCr SQS concentrated ternary alloys.

Layer	NiFeCo (mJ/m^2)	NiCoCr (mJ/m^2)	NiFeCr (mJ/m^2)
1	66.683	-64.289	12.344
2	104.397	70.18	176.292
3	77.941	36.39	80.34
4	52.0572	-43.927	-111.177
5	89.127	74.779	1.268
6	19.935	46.628	-7.319
7	52.978	-51.434	-62.919
8	42.859	-35.738	-57.039
9	85.868	-131.244	32.304

Due to higher concentration of the alloying elements, there is a wider distribution of SFEs and Bader charges as demonstrated by Figure 20. Figure 21 shows a significant increase in bond-length variations compared to dilute ternaries in Figure 16, especially in Cr-containing compositions. The effect of Cr on bond length variation is evident in all bond lengths, especially in Cr-Cr bonds as shown in Figure 21e. The increased concentration of alloying elements leads to a more pronounced distortion which is reflected in the altered shape of the atom. The irregular shapes of the atoms are quantified by image analysis using Fiji software [63]. Specifically, the area occupied by the charge density of an atom, obtained from the pixel occupancy, is calculated. Figure 22 shows the data for all alloys in dilute-binary, dilute-ternary and concentrated-SQS structures. Due to higher symmetry (and little distortion), Figure 22a shows a narrow distribution of atomic areas of Ni and Co atoms. It is also observed that Co atoms are larger than Ni atoms, which is consistent with their metallic radii. Similar narrower distribution is

observed in Ni and Fe atoms in Figure 22b. In contrast, a much wider distribution is observed in Cr atoms in Ni-Cr alloy shown in Figure 22c, as expected based on the above results.

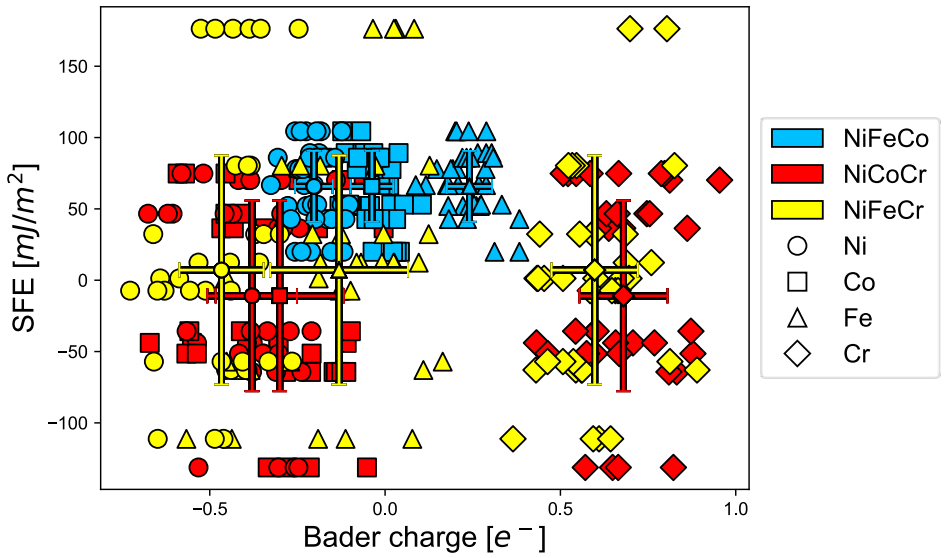

Figure 20. Comparison of SFE and Bader charge variations among NiFeCo, NiCoCr and NiFeCr in the three SQS ternary alloys. The SFEs were calculated for all nine layers in each supercell shown in Figure 5c.

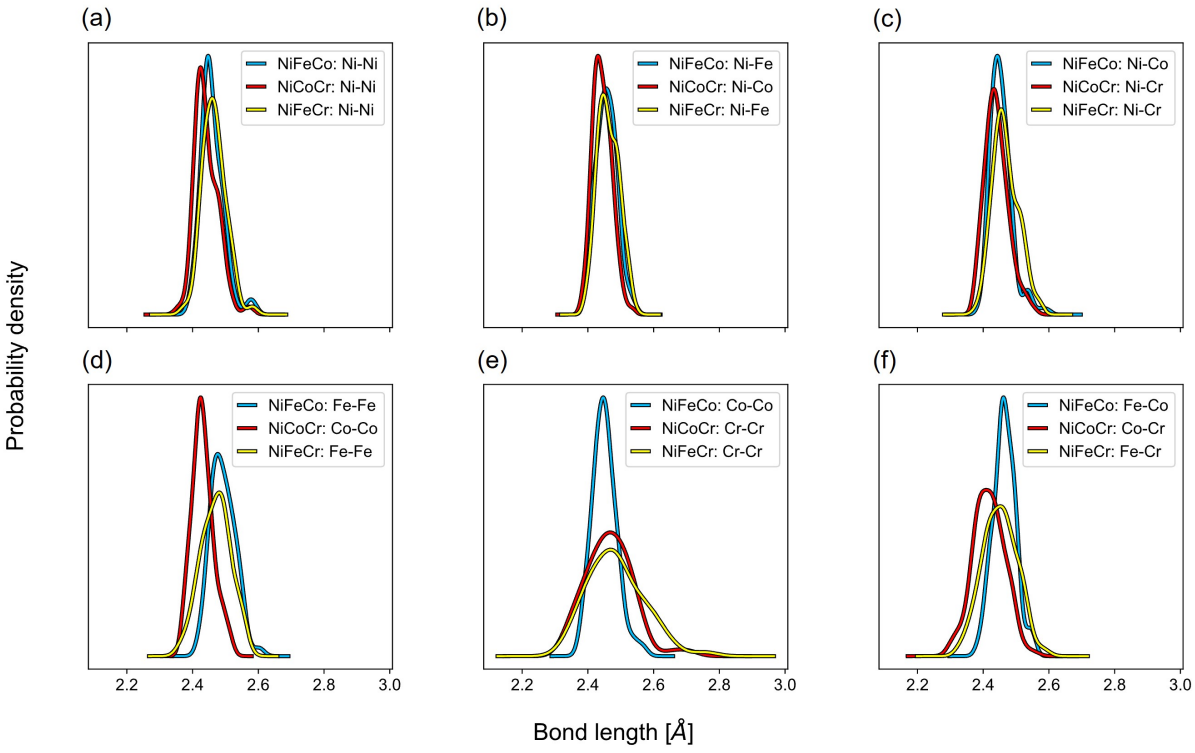

Figure 21. Bond length distribution for all concentrated ternary alloys. Six 1NN bond types are considered for all structures: (a) Ni-Ni, (b) Ni-X_1, (c) Ni-X_2, (d) X_1-X_1, (e) X_2-X_2, (f) X_1-X_2 where X_1 and X_2 represent the distinct alloying elements for each structure.

The distribution widens in dilute ternaries in Cr-containing alloys as shown in Figure 22e and 22f, compared to narrow distribution in NiFeCo as shown in Figure 22d. Interestingly, there is almost no difference between the distributions of binary and dilute ternary compositions as shown in Figure 22a, 22b and 22d. This indicates that the substitution of Co and Fe atoms does not have a significant effect on LCD. In contrast, a significant difference is observed between Cr-containing alloys; the area distribution increases not only for Cr atoms, but also for Ni, Co and Fe, as shown in Figure 22e and 22f compared to binary alloys. Finally, in the concentrated SQS structures, the variations further increase in Cr-containing

alloys, as shown in Figure 22h and 22i, in agreement with the above results. In NiFeCo, the variations widen compared to binary counterparts as shown in Figure 22g, but the widening is not as large as in NiFeCr. The LLD and LCD effects are observed in the SFE values in Table 3; although, due to higher concentration of alloying elements, the SFE variations are larger in all three alloys, but they are significantly larger in Cr-containing NiCoCr and NiFeCr alloys illustrating the additional contribution of LCD.

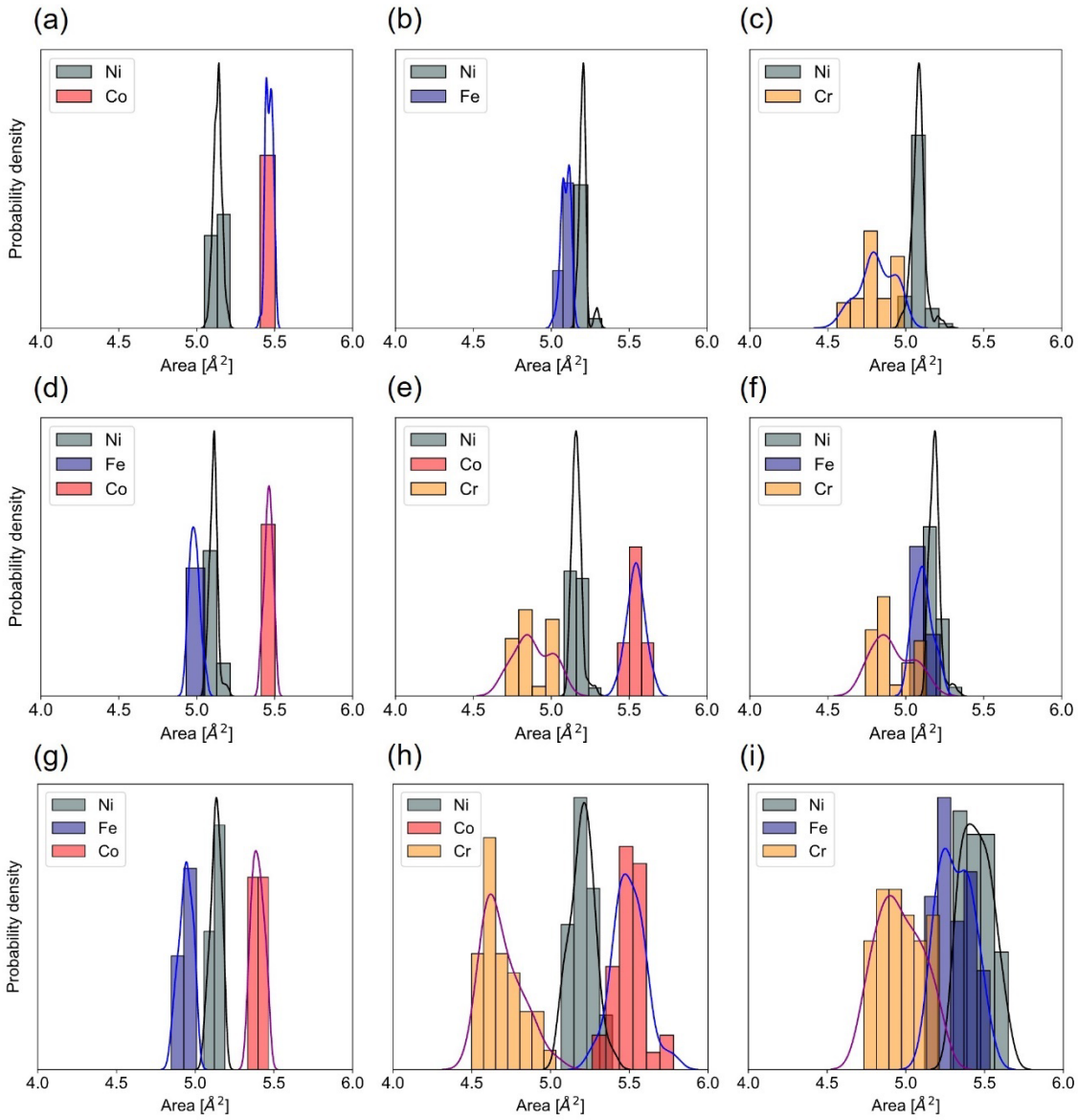

Figure 22. Charge density areas of the atoms in (a) dilute binaries, (b) dilute ternaries, and (c) SQS structures caused by LCD. Wider atomic area distributions are observed in all Cr-containing alloys.

CHAPTER FOUR: DISCUSSION

In this work, the effects of LCD in Ni-based alloys have been studied with particular emphasis on its correlation to SFE variation using DFT calculations. In previous studies, wide ranges of SFEs have been observed in HEAs using DFT methods [27,66–68]. It has been established that this observation is due to the extensive chemical disorder and unique nearest-neighbor environments often found in these alloys. The new results in this work illustrate that the charge density distortion can also have a significant impact on SFE. In NiCo, NiFe, and NiFeCo structures, there are no notable differences in the LCD or SFE despite diverse atomic configurations. Conversely, Cr-containing compositions have wider SFE variations because they exhibit greater charge distortion. As postulated by Zhao et al. [43], Cr has partially filled *d*-orbitals which allows the flexibility to transition from t_{2g} to e_g electronic states that enable easier charge re-distribution. Such redistribution is subdued in other elements. Larger variation of bond lengths and Bader charges due to Cr compared to other elements have been observed that support the findings in this work. Our results demonstrate that the SFE variations that have been observed in previous works can be partly attributed to LCD, rather than solely based on the nearest neighbor environment and LLD. In a previous work in our group, charge density distribution was used as a descriptor for a convolutional neural network (CNN) model to predict SFE in alloys [41,42]. The

integration of ImageJ/Fiji processing tools provides detailed insights to the understanding of the mechanisms governing charge and lattice distortion in alloys.

Short-range order (SRO) has been under intense scrutiny in HEA research. Ding et al. [27] had had revealed that the SFE has a strong correlation with local ordering. They showed that as the degree of SRO increases, the SFE is more likely to converge to positive values in NiCoCr. Similar results are found experimentally in NiCoCr by Zhang et al. [69] where higher SFE is observed in SRO structures. In view of the results in this work, the charge density distortion in SRO vs non-SRO structures and their effects on SFEs need to be probed, which will constitute our future work. It is possible that a random distribution of Cr could lead to a more pronounced asymmetrical charge distribution, potentially causing these SFE fluctuations in non-SRO structures.

An additional layer of complexity emerges when considering the magnetic interactions in these alloys. As demonstrated by Walsh et al. [70], high concentrations of Cr can lead to a highly frustrated magnetic states due to the antiferromagnetic nature of Cr. Despite collinear spin-polarized calculations [25,49,70–72], the impact of disordered magnetic states in these alloys remains an open question. For example, non-collinear calculations by Yu et al. [73] revealed semi-collinear spin moment behavior for Co and Cr atoms in NiCoCr, leading to differences in SFE between paramagnetic and ferromagnetic states. Investigation of the NiFeMnCr structure by Li et al. [72] found that the spins are frustrated due to competing magnetic interactions between the neighboring atoms.

First NN atomic pairings tend to favor antiferromagnetic coupling, while second NN coupling is predominantly ferromagnetic. As noted by Li et al. [72], collinear spin coupling may not be able to accurately describe the magnetic ground state of these types of alloys. Conversely, there have been various studies that have treated NiCoCr as non-spin-polarized or non-magnetic [24,74]. These studies collectively highlight the need to further understand the role of magnetic states on the atomic structure and charge density distribution in HEAs.

CHAPTER FIVE: CONCLUSION/FUTURE WORK

In conclusion, the DFT calculations show that there could be significant charge density distortion around Cr atoms in Ni-based HEAs, compared to relatively little distortion around other elements including Ni, Fe and Co. Consequently, larger lattice distortion is observed in Cr-containing alloys, which results in larger variations in SFEs. These results indicate that local charge distortion may have a significant contribution to local lattice distortion in HEAs.

Future work will focus on the relationship between LCD and the generalized stacking fault energy (GSFE) curve. The GSFE is a measure of the energy barrier experienced when two adjacent planes undergo shear deformation along a specific slip direction on a given slip plane [75]. This energy penalty incorporates both stable and unstable stacking fault configurations, along with twin fault energies. The GSFE curve, compared to a single SFE value, offers a more comprehensive analysis of the energy landscape. This detailed information can be utilized for a diverse range of ab-initio simulations including Peierls-Nabarro and phase-field dislocation models, plastic deformation, crystal growth, phase transition, and twin-twin interactions [75,76]. By applying the image processing techniques described in the *Methodology* section to the GSFE curve, we could gain a more in-depth analysis of how the asymmetric charge distribution influences the activation energies for dislocation motion obtained from the curve.

References

[1] Y.F. Ye, Q. Wang, J. Lu, C.T. Liu, Y. Yang, High-entropy alloy: challenges and prospects, Materials Today 19 (2016) 349–362. https://doi.org/10.1016/j.mattod.2015.11.026.

[2] E.J. Pickering, N.G. Jones, High-entropy alloys: a critical assessment of their founding principles and future prospects, International Materials Reviews 61 (2016) 183–202. https://doi.org/10.1080/09506608.2016.1180020.

[3] N.L. Okamoto, K. Yuge, K. Tanaka, H. Inui, E.P. George, Atomic displacement in the CrMnFeCoNi high-entropy alloy - A scaling factor to predict solid solution strengthening, AIP Adv 6 (2016). https://doi.org/10.1063/1.4971371.

[4] H.S. Oh, K. Odbadrakh, Y. Ikeda, S. Mu, F. Körmann, C.J. Sun, H.S. Ahn, K.N. Yoon, D. Ma, C.C. Tasan, T. Egami, E.S. Park, Element-resolved local lattice distortion in complex concentrated alloys: An observable signature of electronic effects, Acta Mater 216 (2021). https://doi.org/10.1016/j.actamat.2021.117135.

[5] A. Goyal, Y. Li, A. Chernatynskiy, J.S. Jayashankar, M.C. Kautzky, S.B. Sinnott, S.R. Phillpot, The influence of alloying on the stacking fault energy of gold from density functional theory calculations, Comput Mater Sci 188 (2021). https://doi.org/10.1016/j.commatsci.2020.110236.

[6] Y. Zhang, T.T. Zuo, Z. Tang, M.C. Gao, K.A. Dahmen, P.K. Liaw, Z.P. Lu, Microstructures and properties of high-entropy alloys, Prog Mater Sci 61 (2014) 1–93. https://doi.org/10.1016/j.pmatsci.2013.10.001.

[7] J.W. Yeh, S.K. Chen, S.J. Lin, J.Y. Gan, T.S. Chin, T.T. Shun, C.H. Tsau, S.Y. Chang, Nanostructured high-entropy alloys with multiple principal elements: Novel alloy design concepts and outcomes, Adv Eng Mater 6 (2004) 299–303. https://doi.org/10.1002/adem.200300567.

[8] B. Cantor, I.T.H. Chang, P. Knight, A.J.B. Vincent, Microstructural development in equiatomic multicomponent alloys, Materials Science and Engineering: A 375–377 (2004) 213–218. https://doi.org/10.1016/j.msea.2003.10.257.

[9] E.P. George, D. Raabe, R.O. Ritchie, High-entropy alloys, Nat Rev Mater 4 (2019) 515–534. https://doi.org/10.1038/s41578-019-0121-4.

[10] D. Kumar, Recent advances in tribology of high entropy alloys: A critical review, Prog Mater Sci 136 (2023). https://doi.org/10.1016/j.pmatsci.2023.101106.

[11] J. Chen, X. Zhou, W. Wang, B. Liu, Y. Lv, W. Yang, D. Xu, Y. Liu, A review on fundamental of high entropy alloys with promising high–

temperature properties, J Alloys Compd 760 (2018) 15–30. https://doi.org/10.1016/j.jallcom.2018.05.067.
[12] H.S. Oh, D. Ma, G.P. Leyson, B. Grabowski, E.S. Park, F. Kormann, D. Raabe, Lattice distortions in the FeCoNiCrMn high entropy alloy studied by theory and experiment, Entropy 18 (2016). https://doi.org/10.3390/e18090321.
[13] Y.Y. Tan, M.Y. Su, Z.C. Xie, Z.J. Chen, Y. Gong, L.R. Zheng, Z. Shi, G. Mo, Y. Li, L.W. Li, H.Y. Wang, L.H. Dai, Chemical composition dependent local lattice distortions and magnetism in high entropy alloys, Intermetallics (Barking) 129 (2021). https://doi.org/10.1016/j.intermet.2020.107050.
[14] C. Lee, G. Song, M.C. Gao, R. Feng, P. Chen, J. Brechtl, Y. Chen, K. An, W. Guo, J.D. Poplawsky, S. Li, A.T. Samaei, W. Chen, A. Hu, H. Choo, P.K. Liaw, Lattice distortion in a strong and ductile refractory high-entropy alloy, Acta Mater 160 (2018) 158–172. https://doi.org/10.1016/j.actamat.2018.08.053.
[15] P. Wang, Y. Wu, J. Liu, H. Wang, Impacts of atomic scale lattice distortion on dislocation activity in high-entropy alloys, Extreme Mech Lett 17 (2017) 38–42. https://doi.org/10.1016/j.eml.2017.09.015.
[16] J. Mo, X. Liang, B. Shen, Y. Wan, H. Mao, Z. Zhang, W. Li, S. Schönecker, L. Vitos, X. Li, Local lattice distortions, phase stability, and mechanical properties of NbMoTaWHfx alloys: A combined theoretical and experimental study, Comput Mater Sci 217 (2023). https://doi.org/10.1016/j.commatsci.2022.111891.
[17] W. Liu, X.G. Lu, Q.M. Hu, Comprehensive understanding of local lattice distortion in dilute and equiatomic FCC alloys, Mater Chem Phys 293 (2023). https://doi.org/10.1016/j.matchemphys.2022.126928.
[18] Y. Tong, G. Velisa, S. Zhao, W. Guo, T. Yang, K. Jin, C. Lu, H. Bei, J.Y.P. Ko, D.C. Pagan, Y. Zhang, L. Wang, F.X. Zhang, Evolution of local lattice distortion under irradiation in medium- and high-entropy alloys, Materialia (Oxf) 2 (2018) 73–81. https://doi.org/10.1016/j.mtla.2018.06.008.
[19] Y. Tong, S. Zhao, H. Bei, T. Egami, Y. Zhang, F. Zhang, Severe local lattice distortion in Zr- and/or Hf-containing refractory multi-principal element alloys, Acta Mater 183 (2020) 172–181. https://doi.org/10.1016/j.actamat.2019.11.026.
[20] L.J. Santodonato, Y. Zhang, M. Feygenson, C.M. Parish, M.C. Gao, R.J.K. Weber, J.C. Neuefeind, Z. Tang, P.K. Liaw, Deviation from high-entropy configurations in the atomic distributions of a multi-principal-element alloy, Nat Commun 6 (2015). https://doi.org/10.1038/ncomms6964.
[21] H.S. Oh, D. Ma, G.P. Leyson, B. Grabowski, E.S. Park, F. Kormann, D. Raabe, Lattice distortions in the FeCoNiCrMn high entropy alloy

studied by theory and experiment, Entropy 18 (2016). https://doi.org/10.3390/e18090321.
[22] H. Song, F. Tian, Q.M. Hu, L. Vitos, Y. Wang, J. Shen, N. Chen, Local lattice distortion in high-entropy alloys, Phys Rev Mater 1 (2017). https://doi.org/10.1103/PhysRevMaterials.1.023404.
[23] H.S. Oh, S.J. Kim, K. Odbadrakh, W.H. Ryu, K.N. Yoon, S. Mu, F. Körmann, Y. Ikeda, C.C. Tasan, D. Raabe, T. Egami, E.S. Park, Engineering atomic-level complexity in high-entropy and complex concentrated alloys, Nat Commun 10 (2019). https://doi.org/10.1038/s41467-019-10012-7.
[24] H.S. Oh, K. Odbadrakh, Y. Ikeda, S. Mu, F. Körmann, C.J. Sun, H.S. Ahn, K.N. Yoon, D. Ma, C.C. Tasan, T. Egami, E.S. Park, Element-resolved local lattice distortion in complex concentrated alloys: An observable signature of electronic effects, Acta Mater 216 (2021). https://doi.org/10.1016/j.actamat.2021.117135.
[25] C. Niu, C.R. LaRosa, J. Miao, M.J. Mills, M. Ghazisaeidi, Magnetically-driven phase transformation strengthening in high entropy alloys, Nat Commun 9 (2018). https://doi.org/10.1038/s41467-018-03846-0.
[26] S. Zhao, G.M. Stocks, Y. Zhang, Stacking fault energies of face-centered cubic concentrated solid solution alloys, Acta Mater 134 (2017) 334–345. https://doi.org/10.1016/j.actamat.2017.05.001.
[27] J. Ding, Q. Yu, M. Asta, R.O. Ritchie, Tunable stacking fault energies by tailoring local chemical order in CrCoNi medium-entropy alloys, Proc Natl Acad Sci U S A 115 (2018) 8919–8924. https://doi.org/10.1073/pnas.1808660115.
[28] M. Shih, J. Miao, M. Mills, M. Ghazisaeidi, Stacking fault energy in concentrated alloys, Nat Commun 12 (2021). https://doi.org/10.1038/s41467-021-23860-z.
[29] D. Hull, D.J. Bacon, Introduction to Dislocations, Butterworth-Heinemann, Oxford, 2011. http://libproxy.clemson.edu/login?url=https://search.ebscohost.com/login.aspx?direct=true&db=e025xna&AN=379941.
[30] S.F. Liu, Y. Wu, H.T. Wang, J.Y. He, J.B. Liu, C.X. Chen, X.J. Liu, H. Wang, Z.P. Lu, Stacking fault energy of face-centered-cubic high entropy alloys, Intermetallics (Barking) 93 (2018) 269–273. https://doi.org/10.1016/j.intermet.2017.10.004.
[31] S. Zhao, Y. Osetsky, G.M. Stocks, Y. Zhang, Local-environment dependence of stacking fault energies in concentrated solid-solution alloys, NPJ Comput Mater 5 (2019). https://doi.org/10.1038/s41524-019-0150-y.
[32] S.L. Shang, C.L. Zacherl, H.Z. Fang, Y. Wang, Y. Du, Z.K. Liu, Effects of alloying element and temperature on the stacking fault energies of dilute Ni-base superalloys, Journal of Physics

Condensed Matter 24 (2012). https://doi.org/10.1088/0953-8984/24/50/505403.
[33] S.H. Zhang, I.J. Beyerlein, D. Legut, Z.H. Fu, Z. Zhang, S.L. Shang, Z.K. Liu, T.C. Germann, R.F. Zhang, First-principles investigation of strain effects on the stacking fault energies, dislocation core structure, and Peierls stress of magnesium and its alloys, Phys Rev B 95 (2017). https://doi.org/10.1103/PhysRevB.95.224106.
[34] S. Ogata, J. Li, S. Yip, Ideal Pure Shear Strength of Aluminum and Copper, Science (1979) 298 (2002) 807–811. https://doi.org/10.1126/science.1076652.
[35] Y.F. Wu, S. Li, Z.G. Ding, W. Liu, Y.H. Zhao, Y.T. Zhu, Effect of charge redistribution factor on stacking-fault energies of Mg-based binary alloys, Scr Mater 112 (2016) 101–105. https://doi.org/10.1016/j.scriptamat.2015.09.023.
[36] T.L. Achmad, W. Fu, H. Chen, C. Zhang, Z.G. Yang, Computational thermodynamic and first-principles calculation of stacking fault energy on ternary Co-based alloys, Comput Mater Sci 143 (2018) 112–117. https://doi.org/10.1016/j.commatsci.2017.11.004.
[37] M. Krčmar, C.L. Fu, A. Janotti, R.C. Reed, Diffusion rates of 3d transition metal solutes in nickel by first-principles calculations, Acta Mater 53 (2005) 2369–2376. https://doi.org/10.1016/j.actamat.2005.01.044.
[38] R.B. Araujo, I. Bayrak Pehlivan, T. Edvinsson, High-entropy alloy catalysts: Fundamental aspects, promises towards electrochemical NH3 production, and lessons to learn from deep neural networks, Nano Energy 105 (2023). https://doi.org/10.1016/j.nanoen.2022.108027.
[39] J. Hao, Z. Zhuang, K. Cao, G. Gao, C. Wang, F. Lai, S. Lu, P. Ma, W. Dong, T. Liu, M. Du, H. Zhu, Unraveling the electronegativity-dominated intermediate adsorption on high-entropy alloy electrocatalysts, Nat Commun 13 (2022). https://doi.org/10.1038/s41467-022-30379-4.
[40] Y. Sun, S. Dai, High-entropy materials for catalysis: A new frontier, Sci Adv 7 (2021). https://doi.org/10.1126/sciadv.abg1600.
[41] G. Arora, S. Kamrava, P. Tahmasebi, D.S. Aidhy, Charge-density based convolutional neural networks for stacking fault energy prediction in concentrated alloys, Materialia (Oxf) 26 (2022). https://doi.org/10.1016/j.mtla.2022.101620.
[42] G. Arora, A. Manzoor, D.S. Aidhy, Charge-density based evaluation and prediction of stacking fault energies in Ni alloys from DFT and machine learning, J Appl Phys 132 (2022). https://doi.org/10.1063/5.0122675.
[43] S. Zhao, T. Egami, G.M. Stocks, Y. Zhang, Effect of d electrons on defect properties in equiatomic NiCoCr and NiCoFeCr concentrated

solid solution alloys, Phys Rev Mater 2 (2018). https://doi.org/10.1103/PhysRevMaterials.2.013602.
[44] G. Kresse, J. Hafner, Ab initio molecular dynamics for liquid metals, Phys Rev B 47 (1993) 558–561. https://doi.org/10.1103/PhysRevB.47.558.
[45] G. Kresse, J. Furthmüller, Efficient iterative schemes for ab initio total-energy calculations using a plane-wave basis set, Phys Rev B 54 (1996) 11169–11186. https://doi.org/10.1103/PhysRevB.54.11169.
[46] G. Kresse, J. Furthmüller, Efficiency of ab-initio total energy calculations for metals and semiconductors using a plane-wave basis set, Comput Mater Sci 6 (1996) 15–50. https://doi.org/https://doi.org/10.1016/0927-0256(96)00008-0.
[47] G. Kresse, D. Joubert, From ultrasoft pseudopotentials to the projector augmented-wave method, Phys Rev B 59 (1999) 1758–1775. https://doi.org/10.1103/PhysRevB.59.1758.
[48] A. van de Walle, Multicomponent multisublattice alloys, nonconfigurational entropy and other additions to the Alloy Theoretic Automated Toolkit, CALPHAD 33 (2009) 266–278. https://doi.org/10.1016/j.calphad.2008.12.005.
[49] D. Ma, B. Grabowski, F. Körmann, J. Neugebauer, D. Raabe, Ab initio thermodynamics of the CoCrFeMnNi high entropy alloy: Importance of entropy contributions beyond the configurational one, Acta Mater 100 (2015) 90–97. https://doi.org/10.1016/j.actamat.2015.08.050.
[50] A. Tamm, A. Aabloo, M. Klintenberg, M. Stocks, A. Caro, Atomic-scale properties of Ni-based FCC ternary, and quaternary alloys, Acta Mater 99 (2015) 307–312. https://doi.org/10.1016/j.actamat.2015.08.015.
[51] B. Yin, S. Yoshida, N. Tsuji, W.A. Curtin, Yield strength and misfit volumes of NiCoCr and implications for short-range-order, Nat Commun 11 (2020). https://doi.org/10.1038/s41467-020-16083-1.
[52] C. Niu, A.J. Zaddach, A.A. Oni, X. Sang, J.W. Hurt, J.M. Lebeau, C.C. Koch, D.L. Irving, Spin-driven ordering of Cr in the equiatomic high entropy alloy NiFeCrCo, Appl Phys Lett 106 (2015). https://doi.org/10.1063/1.4918996.
[53] S.L. Shang, W.Y. Wang, B.C. Zhou, Y. Wang, K.A. Darling, L.J. Kecskes, S.N. Mathaudhu, Z.K. Liu, Generalized stacking fault energy, ideal strength and twinnability of dilute Mg-based alloys: A first-principles study of shear deformation, Acta Mater 67 (2014) 168–180. https://doi.org/10.1016/j.actamat.2013.12.019.
[54] P. Tu, Y. Zheng, C. Zhuang, X. Zeng, H. Zhu, A high-throughput computation framework for generalized stacking fault energies of

pure metals, Comput Mater Sci 159 (2019) 357–364. https://doi.org/10.1016/j.commatsci.2018.12.013.
[55] S.L. Shang, W.Y. Wang, Y. Wang, Y. Du, J.X. Zhang, A.D. Patel, Z.K. Liu, Temperature-dependent ideal strength and stacking fault energy of fcc Ni: A first-principles study of shear deformation, Journal of Physics Condensed Matter 24 (2012). https://doi.org/10.1088/0953-8984/24/15/155402.
[56] S.L. Shang, J. Shimanek, S. Qin, Y. Wang, A.M. Beese, Z.K. Liu, Unveiling dislocation characteristics in N i3Al from stacking fault energy and ideal strength: A first-principles study via pure alias shear deformation, Phys Rev B 101 (2020). https://doi.org/10.1103/PhysRevB.101.024102.
[57] X. Zhang, B. Grabowski, F. Körmann, A. V. Ruban, Y. Gong, R.C. Reed, T. Hickel, J. Neugebauer, Temperature dependence of the stacking-fault Gibbs energy for Al, Cu, and Ni, Phys Rev B 98 (2018). https://doi.org/10.1103/PhysRevB.98.224106.
[58] D.J. Siegel, Generalized stacking fault energies, ductilities, and twinnabilities of Ni and selected Ni alloys, Appl Phys Lett 87 (2005) 1–3. https://doi.org/10.1063/1.2051793.
[59] M. Chandran, S.K. Sondhi, First-principle calculation of stacking fault energies in Ni and Ni-Co alloy, in: J Appl Phys, 2011. https://doi.org/10.1063/1.3585786.
[60] W. Li, X. Peng, A.H.W. Ngan, J.A. El-Awady, Surface energies and relaxation of NiCoCr and NiFeX (X = Cu, Co or Cr) equiatomic multiprincipal element alloys from first principles calculations, Model Simul Mat Sci Eng 30 (2022). https://doi.org/10.1088/1361-651X/ac3e07.
[61] G. Arora, D.S. Aidhy, Machine learning enabled prediction of stacking fault energies in concentrated alloys, Metals (Basel) 10 (2020) 1–17. https://doi.org/10.3390/met10081072.
[62] N. Papior, sisl: v<fill-version>, (2023). https://doi.org/10.5281/zenodo.597181.
[63] J. Schindelin, I. Arganda-Carreras, E. Frise, V. Kaynig, M. Longair, T. Pietzsch, S. Preibisch, C. Rueden, S. Saalfeld, B. Schmid, J.Y. Tinevez, D.J. White, V. Hartenstein, K. Eliceiri, P. Tomancak, A. Cardona, Fiji: An open-source platform for biological-image analysis, Nat Methods 9 (2012) 676–682. https://doi.org/10.1038/nmeth.2019.
[64] J. Pijuan, C. Barceló, D.F. Moreno, O. Maiques, P. Sisó, R.M. Marti, A. Macià, A. Panosa, In vitro cell migration, invasion, and adhesion assays: From cell imaging to data analysis, Front Cell Dev Biol 7 (2019). https://doi.org/10.3389/fcell.2019.00107.
[65] J.W. Boley, E.L. White, R.K. Kramer, Mechanically sintered gallium-indium nanoparticles, Advanced Materials 27 (2015) 2355–2360. https://doi.org/10.1002/adma.201404790.

[66] Y. Ikeda, F. Körmann, I. Tanaka, J. Neugebauer, Impact of chemical fluctuations on stacking fault energies of CrCoNi and CrMnFeCoNi high entropy alloys from first principles, Entropy 20 (2018). https://doi.org/10.3390/e20090655.
[67] P. Singh, S. Picak, A. Sharma, Y.I. Chumlyakov, R. Arroyave, I. Karaman, D.D. Johnson, Martensitic Transformation in FexMn80-xCo10Cr10 High-Entropy Alloy, Phys Rev Lett 127 (2021). https://doi.org/10.1103/PhysRevLett.127.115704.
[68] Y.C. Yang, C. Liu, C.Y. Lin, Z. Xia, Core effect of local atomic configuration and design principles in AlxCoCrFeNi high-entropy alloys, Scr Mater 178 (2020) 181–186. https://doi.org/10.1016/j.scriptamat.2019.11.016.
[69] R. Zhang, S. Zhao, J. Ding, Y. Chong, T. Jia, C. Ophus, M. Asta, R.O. Ritchie, A.M. Minor, Short-range order and its impact on the CrCoNi medium-entropy alloy, Nature 581 (2020) 283–287. https://doi.org/10.1038/s41586-020-2275-z.
[70] F. Walsh, M. Asta, R. Ritchie, Magnetically driven short-range order can explain anomalous measurements in CrCoNi, Proceedings of the National Academy of Sciences 118 (2021) e2020540118. https://doi.org/10.1073/pnas.2020540118.
[71] C. Wagner, A. Ferrari, J. Schreuer, J.P. Couzinié, Y. Ikeda, F. Körmann, G. Eggeler, E.P. George, G. Laplanche, Effects of Cr/Ni ratio on physical properties of Cr-Mn-Fe-Co-Ni high-entropy alloys, Acta Mater 227 (2022). https://doi.org/10.1016/j.actamat.2022.117693.
[72] C. Li, J. Yin, K. Odbadrakh, B.C. Sales, S.J. Zinkle, G.M. Stocks, B.D. Wirth, First principle study of magnetism and vacancy energetics in a near equimolar NiFeMnCr high entropy alloy, J Appl Phys 125 (2019). https://doi.org/10.1063/1.5086172.
[73] P. Yu, J.P. Du, S. Shinzato, F.S. Meng, S. Ogata, Theory of history-dependent multi-layer generalized stacking fault energy— A modeling of the micro-substructure evolution kinetics in chemically ordered medium-entropyalloys, Acta Mater 224 (2022). https://doi.org/10.1016/j.actamat.2021.117504.
[74] B.C. Sales, K. Jin, H. Bei, G.M. Stocks, G.D. Samolyuk, A.F. May, M.A. McGuire, Quantum Critical Behavior in a Concentrated Ternary Solid Solution, Sci Rep 6 (2016). https://doi.org/10.1038/srep26179.
[75] S.L. Shang, W.Y. Wang, B.C. Zhou, Y. Wang, K.A. Darling, L.J. Kecskes, S.N. Mathaudhu, Z.K. Liu, Generalized stacking fault energy, ideal strength and twinnability of dilute Mg-based alloys: A first-principles study of shear deformation, Acta Mater 67 (2014) 168–180. https://doi.org/10.1016/j.actamat.2013.12.019.
[76] A.R. Natarajan, A. Van der Ven, Linking electronic structure calculations to generalized stacking fault energies in multicomponent

alloys, NPJ Comput Mater 6 (2020). https://doi.org/10.1038/s41524-020-0348-z.